IEEE Access
Multidisciplinary | Rapid Review | Open Access Journal

Received 3 July 2022, accepted 23 July 2022, date of publication 1 August 2022, date of current version 5 August 2022.

Digital Object Identifier 10.1109/ACCESS.2022.3195494

RESEARCH ARTICLE

Comparison of PLL-Based and PLL-Less Control Strategies for Grid-Following Inverters Considering Time and Frequency Domain Analysis

NABIL MOHAMMED, (Member, IEEE), WEIHUA ZHOU, (Member, IEEE), AND BEHROOZ BAHRANI, (Senior Member, IEEE)

Department of Electrical and Computer Systems Engineering, Monash University, Melbourne, VIC 3800, Australia

Corresponding author: Weihua Zhou (weihua.zhou@monash.edu)

This work was supported in part by the Monash Grid Innovation Hub, and in part by the Australian Renewable Energy Agency (ARENA) through the Advancing Renewable Program under Grant 2020/ARP007.

ABSTRACT This article presents a comprehensive comparison of three control strategies used for grid-following inverters (GFLIs). The first strategy is the phase-locked loop (PLL)-based vector current control (VCC), and the other two PLL-less controllers are the voltage-modulated direct power control (VMDPC) and the linear-parameter-varying power-synchronized control (LPV-PSC). The VCC relies on the PLL to synchronize with the grid frequency to control the exchanged real and reactive power with the grid, which may result in instability issues under weak grid conditions. To prevent this, the VMDPC and LPV-PSC are proposed recently as PLL-less approaches to overcome the difficulties of the VCC in weak grid conditions. The performances of the VCC, VMDPC, and LPV-PSC are comprehensively reviewed in this article, considering the operations of the GFLIs under both strong and weak grids. In each operation mode, the provided tests investigate: 1) step response of active and reactive power, 2) frequency jump in the grid voltage source, 3) phase jump in the grid voltage source, and 4) voltage sag in the grid voltage source. In addition to evaluating the three controllers in the time-domain, the frequency-domain impedance-based stability analysis based on the generalized Nyquist criterion is also considered, which confirms the time-domain findings in terms of accurate predictions of the stable/unstable operations of the GFLIs that are equipped with these controllers. It is found that, compared to the conventional VCC and the VMDPC, the LPV-PSC has promising performance under various test conditions in both strong and weak grids, which may be a future solution for weak-grids connection of the GFLIs.

INDEX TERMS Direct power control, grid-following inverters, linear-parameter-varying control, power-synchronized inverters, stability, vector current control.

I. INTRODUCTION

The rapid developments of renewable energy technologies have significantly accelerated the integration of inverter-based resources (IBRs) into the existing power systems. The main advantages of such IBRs are their high reliability, high energy conversion efficiency, and fast dynamic response. Furthermore, the IBRs are flexible as they can be integrated into different voltage levels such as medium voltage (e.g., solar and wind farms) and low voltage distribution networks (e.g., rooftop PV systems). Additionally, the control of these inverters can be configured to enable either islanded operations or grid-connected operations.

On the one hand, in the islanded mode, the main objective of the IBRs is to regulate the microgrid voltage and frequency to their desired commands. On the other hand,

The associate editor coordinating the review of this manuscript and approving it for publication was Pinjia Zhang.

This work is licensed under a Creative Commons Attribution 4.0 License. For more information, see https://creativecommons.org/licenses/by/4.0/

in the grid-connected mode, the IBRs control the injected active power to the grid according to either the desired set-points (e.g., grid-connected battery energy storage systems) or the available power capacity at the DC side (e.g., PV systems). Besides active power injection, the IBRs operating in grid-connected mode can provide ancillary services to the grid [1], such as reactive power injection, low-order harmonic compensation [2], fault ride through [3], voltage imbalance correction [4], and anti-islanding detection [5]. This article focuses on the IBRs operation in the grid-connected mode, where it is also expected that the IBRs should be resilient and flexible to adapt to various abnormal operating conditions, including frequency jumps and voltage sags.

Various control techniques are proposed for grid-connected voltage source converters. These control methods are being implemented either in the stationary reference frame ($\alpha\beta 0$) or in the synchronous (dq) reference frame [6]. While these two reference frames enable independent control of the injected active and reactive power to the grid, the dq reference frame is preferred due to its simplicity. In the dq reference frame, the control signals, i.e., current and voltage, appear as dc quantities that are rotating at the grid fundamental frequency. The conventional vector current control (VCC) is widely used in the literature to control grid-connected inverters [7], [8]. Realization of the VCC is based on the widely-used phase-locked loop (PLL) synchronized with the grid frequency. The VCC is designed in the dq reference frame in which proportional-integral (PI)-based controllers can be used to control the d- and q-axis currents independently; hence, the injected active and reactive power to the grid, independently.

While the VCC-based inverters seamlessly operate in normal conditions of strong grids and enable the export of the maximum power, their performance deteriorates under abnormal operating conditions, such as the occurrence of an unbalanced grid voltage that results in uncontrollable oscillations in the dq-reference frame at double the grid fundamental frequency [9]. Most notably, the control capability of the VCC deteriorates significantly in weak grids, as it relies on the PLL that may eventually lead to instability issues in very weak grids [10]. These raised challenges are becoming more concerning with the continuous and fast-increasing penetration of IBRs and the recommendations worldwide to phase out coal-based power stations, which leads to undesired system strength reduction.

To obviate the shortcomings of the PLL-based VCC, several PLL-less control methods are developed for IBRs. For example, the voltage-modulated direct power control (VMDPC) is proposed in [11], where the DPC concept is initially proposed in [12]. Another PLL-less control method proposed recently is the linear-parameter-varying power-synchronized control (LPV-PSC) [13]. Compared with the conventional VCC approach, the VMDPC does not require a PLL. Therefore, the associated instability problems with PLLs are eliminated. However, the performance of the VMDPC in a weak grid can deteriorate, as it still requires the point-of-common-coupling (PCC) voltage to control the

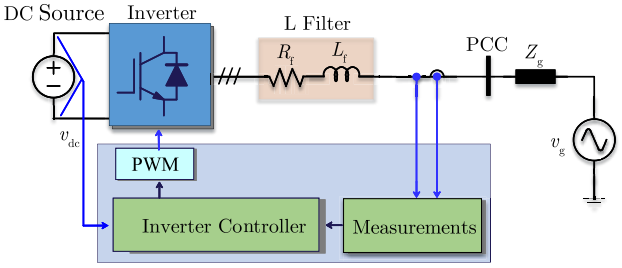

FIGURE 1. Simplified structure of a single-line diagram of a three-phase grid-connected inverter.

power exchange with the grid that significantly affects the PCC voltage [14]. The LPV-PSC for the grid-following inverter (GFLI) also does not use a PLL [13]. This control approach offers several advantages, such as its capabilities for operation in both strong and weak grids. Additionally, the operation of the LPV-PSC is preserved in all operating points.

Although a comprehensive investigation of the performance of the PLL-based VCC and the PLL-less VMDPC is recently presented in [15], the comparisons are only conducted in the time-domain and only by considering the VCC and the VMDPC. Therefore, there is a need for a detailed comparison between the conventional PLL-based VCC, the PLL-less VMDPC, and the PLL-less LPV-PSC, which evaluates the performance of these control systems in both time-domain and frequency-domain. Furthermore, in recent literature, the frequency-domain stability assessment of IBRs, mainly using the impedance-based stability criterion, is proven to accurately predict system stability [16]–[19].

This article comprehensively evaluates the performance of the aforementioned three control strategies: the PLL-based VCC, the PLL-less VMDPC, and the PLL-less LPV-PSC control systems for the GFLIs. First, the performance of the three controllers is tested in strong grid conditions under normal and severe operating conditions, such as step change of power reference commands, frequency jump, phase jump, sag in the PCC voltage, and faults in the PCC. Second, the control strategies are tested under similar test conditions in weak grid conditions. Finally, the impedance-based stability analysis based on the Generalized Nyquist Criterion (GNC) is performed to confirm these time-domain simulation results obtained under both strong and weak grid conditions. The obtained frequency-domain stability conclusions verify the correctness of the time-domain simulation results.

The rest of this article is organized as follows. Section II briefly describes the three control strategies for the GFLIs that are considered in this article. Section III presents a comprehensive time-domain comparison among the three controllers with different operating points under strong and weak grid conditions. In Section IV, the frequency-domain impedance-based analysis is performed to verify the time-domain analysis results. Based on the time-domain and frequency-domain analysis results, Section V summarizes the findings in both the time- and frequency- domains and provides some

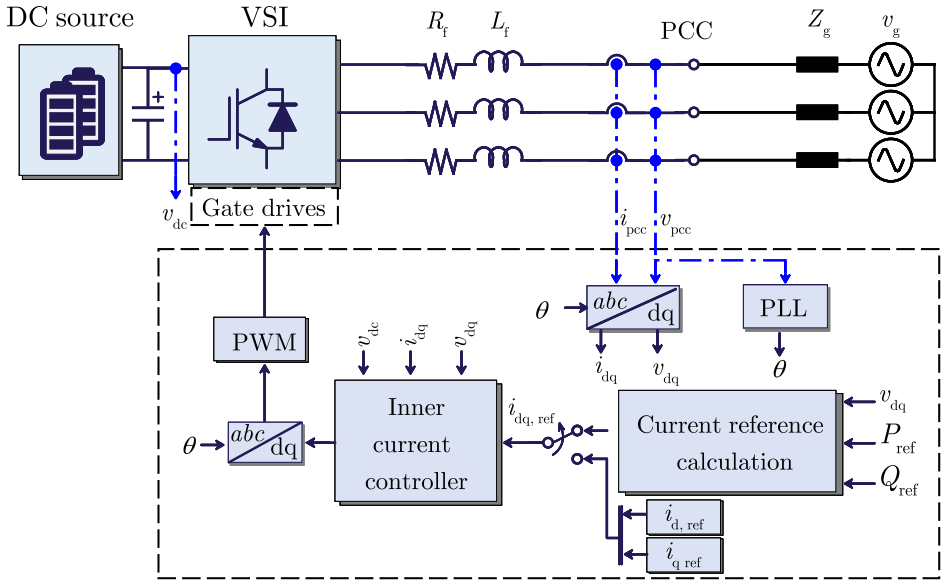

FIGURE 2. Block diagram of a grid-connected VSI equipped with vector-current control [15].

practical application guidelines. Finally, Section VI draws the conclusions of this article.

II. GRID-FOLLOWING CONTROLLER MODELS

To evaluate the performance of the three different control strategies, these control algorithms are implemented into the control loop of three identical GFLIs with the same power rating. These controllers are the standard VCC equipped with an open-loop power control strategy, the VMDPC, and the LPV-PSC control. The system under study is a two-level three-phase voltage source inverter (VSI), as shown in Fig. 1. The VSI is interfaced with the utility grid using an L-filter denoted by L_f with an internal resistance R_f. The three-phase voltages (v_{pcc}) and currents (i_{pcc}) at the PCC are measured and used in the feedback controller and also in the calculation of the exported active (P_{pcc}) and reactive (Q_{pcc}) power to the grid. The grid is modelled as an ideal voltage source with an equivalent Thevenin impedance consisting of the grid resistance R_g and the grid inductance L_g. Further details on the three controller models are discussed below.

A. VECTOR CURRENT CONTROL

Fig. 2 shows the IBR equipped with the conventional VCC. The main goal of the controller is to regulate the PCC current (or power) exchange with the grid to the desired reference commands, $i_{dq,\ ref}$ and $i_{dq,\ ref}$ (or P_{ref} and Q_{ref}), which are generated by external power control loops. The main difference between the VCC and the other two control models used for comparison purposes in this article is the synchronization method with the grid. The VCC is a PLL-based method, whereas both the VMDPC and LPV-PSC are PLL-less control strategies.

The VCC is implemented in the dq reference frame, where the synchronous reference frame PLL (SRF-PLL) is commonly used to extract the phase angle $\theta = \omega t$ of the grid voltage measured at the PCC. Its work principle is to force the q-component of this voltage to zero. Consequently, decoupling of the real and reactive power control is achieved. Therefore, the control contains two decoupled control axes, i.e., the d-component for the active power control and the q-component for the reactive power control. In the literature, it is recommended to design the SRF-PLL with a cut-off frequency around tens of Hertz [20]. Hence, in this article, the PI controller gains are selected $K_{p-pll} = 0.292$ and $K_{i-pll} = 42.2$, providing a cut off frequency of 50 Hz and a phase margin of 65°.

As shown in Fig. 2, it can be seen that the dq current references ($i_{dq,\ ref}$) for the VCC are either specified directly or generated from the outer open-loop power control (OLPC). The inputs for the OLPC are the desired power references (P_{ref} and Q_{ref}), and the d and q components of the measured PCC voltage (V_d and V_q). These measured components can be used directly for the current reference calculations, or they can be filtered first using low-pass filters (LPF). In this article, both cases of using V_d and V_q without/with LPF are investigated. For the second case, V_d and V_q filtering is realized using a second-order LPF with a transfer function as

$$G_{LPF}(s) = \frac{\omega_f^2}{s^2 + 2\zeta_{LPF}\omega_f s + {\omega_f}^2}, \tag{1}$$

where the damping ratio and the natural frequency are designed as $\zeta_{LPF} = 0.7$ and $\omega_f = 2\pi 200$ rad/s, respectively.

Section IV-A compares the time-domain performance of the three approaches to generate the current reference commands in the dq reference frame ($i_{d,\ ref}$ and $i_{q,\ ref}$). In addition to the analysis in the time-domain, further insights on the

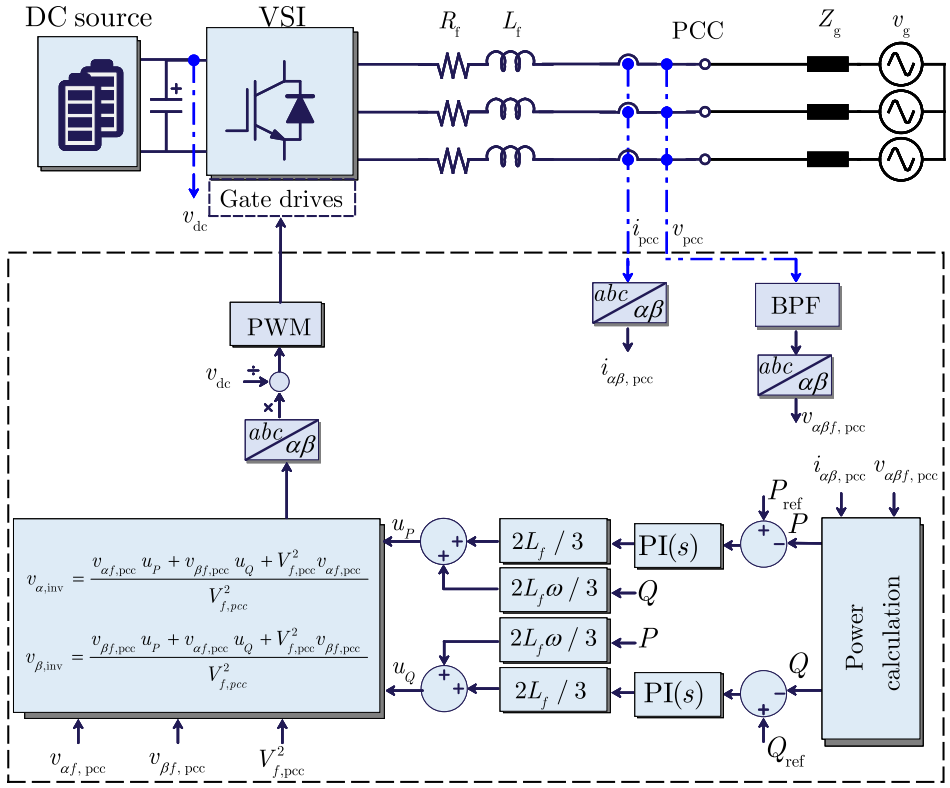

FIGURE 3. Block diagram of a grid-connected VSI equipped with the voltage-modulated direct power control [11].

stability and these differences between the OLPC with and without the LPF used to filter V_d and V_q are explored in the frequency-domain, as shown in Section III.

B. DIRECT POWER CONTROL

Fig. 3 shows the control structure of the VMDPC proposed for GFLIs connected to weak grids [11]. In this control, the PLL is eliminated. For weak-grid applications, it is required to filter out the noise and low-frequency harmonics of the PCC grid voltage. Hence, a standard second-order bandpass filter (BPF) is used to obtain the fundamental-frequency component of the measured PCC voltages. If ω_o is the grid nominal frequency, the transfer function of the RPF can be derived as

$$G_{\mathrm{BPF}}(s) = \frac{2\zeta\omega_o s}{s^2 + 2\zeta_{BPF}\omega_o s + {\omega_o}^2}, \tag{2}$$

where ζ_{BPF} is a damping ratio of the BPF.

C. LINEAR-PARAMETER-VARYING POWER-SYNCHRONIZED CONTROL

Fig. 4 shows the control structure of the LPV-PSC. It is a PLL-less control approach that is proposed recently for both very weak and strong grid conditions without being prone to instability [13]. The LPV-PSC control method regulates the output active and reactive power at the inverter terminal instead of the PCC, similar to the power-synchronized grid-following inverter [14].

The LPV-PSC loop-shaping controller is a class of nonlinear systems. The system parameters are a function of some scheduling variables that can be measured in real-time operation. A nonlinear system that is linearized around some operating points is called an LPV-PSC system, in which the scheduling variables are the operating point parameters [21]. The parameters of the LPV-PSC controller are tuned automatically in real time according to the variation of the operating points, maintaining a constant rise time for different operating points, and a straightforward control design based on the IBR operating point [13].

It is worth mentioning that the main purpose of this article is to provide a comprehensive comparison of the above three control strategies in frequency and time-domain. The interested reader can refer to the literature review for the theoretical models of these existing control strategies.

III. FREQUENCY-DOMAIN RESULTS

The performance of the VCC, VMDPC, and LPV-PSC strategies shown in Fig. 2, Fig. 3, and Fig. 4 are evaluated in the frequency-domain using the impedance-based stability analysis method. The parameters of the three control systems are listed in Table 1.

It is worth mentioning that this article adopted the impedance-based approach to evaluate the stability of

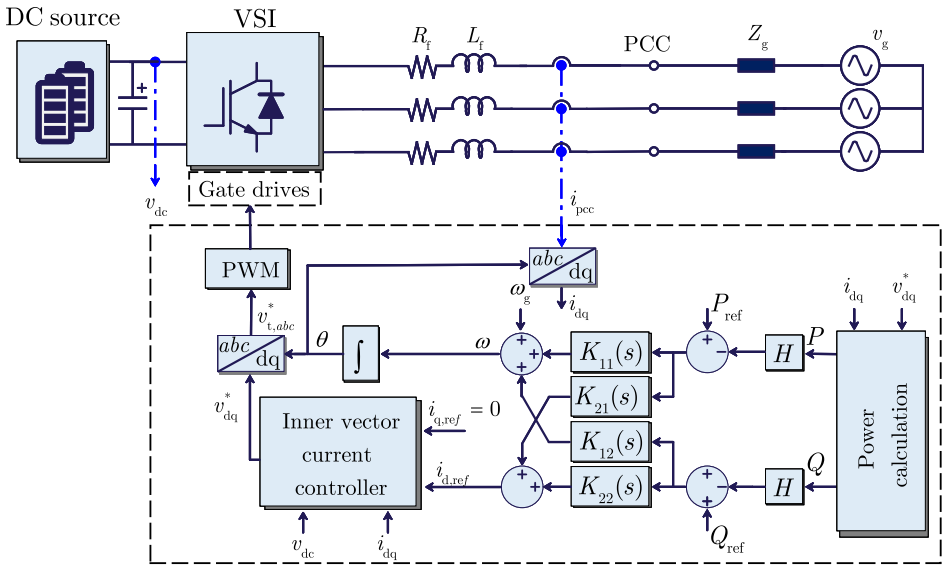

FIGURE 4. Block diagram of a grid-connected VSI equipped with the linear-parameter-varying power-synchronized control [13].

TABLE 1. Parameters of system used for the comparison study.

Paramter	Symbol	Value	Unit
Utility Grid			
Grid voltage (RMS, L-N)	V_g	690	V
Grid frequency	f_g	50	Hz
Strong grid (SCR= 16.8)	R_g	5.4	mΩ
	L_g	51	μH
Weak grid (SCR= 3.12)	R_g	38.9	mΩ
	L_g	254	μH
Very weak grid (SCR= 1.12)	R_g	72	mΩ
	L_g	680	μH
Inverter			
Rated active power	P_n	4	MW
Rated reactive power	Q_n	3	MVar
L-filter inductance	L_f	95	μH
ESR of L-filter inductance	R_f	0.01	Ω
Vector-current Control (VCC)			
Inner current controller gains	K_{p-cc}	0.365	-
	K_{i-cc}	38.5	1/s
SRF-PLL controller gains	K_{p-pll}	0.292	-
	K_{i-pll}	42.2	1/s
Voltage-modulated Direct Power Control (VMDPC)			
Active power controller gains	K_{P-p}	0.4576	-
	K_{P-i}	220.4431	1/s
Reactive power controller gains	K_{Q-p}	0.4576	-
	K_{Q-i}	220.4431	1/s
Resonance frequency of the BPF	ω_0	314.16	rad/s
Damping ratio of the BPF	ζ_{BPF}	0.7	-
linear-parameter-varying power-synchronized control (LPV-PSC)			
Power controller gain	K_P	80	-
Inner current controller gains	$K_{p-LPV-PSC}$	0.365	-
	$K_{i-LPV-PSC}$	38.5	1/s
Power Measurement LPF Bandwidth	f_{fil}	200	Hz

the three controllers in the frequency-domain as it is a well-known modelling strategy and it predicts the stability

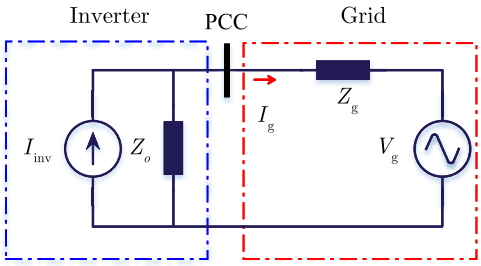

FIGURE 5. Small-signal impedance representation of an GFLI.

accurately. However, other frequency-based strategies, such as eigenvalue analysis, can be used.

The working principle of the impedance-based stability analysis relies on dividing the system under investigation into two parts, i.e., the source and load parts [22]. For the study of grid-connected inverter systems, the inverters are considered the source, while the utility grid is considered the load [16].

Fig. 5 shows the small-signal model of a grid-connected inverter system. The grid-connected inverter is represented by the Norton equivalent circuit that consists of an ideal current source (I_{inv}) and an output impedance (Z_o) connected in parallel with the current source. The grid is modelled by the Thevenin equivalent circuit consisting of an ideal voltage source (V_g) in series with the grid impedance (Z_g). The current flowing from the inverter to the grid is expressed as follows:

$$I_g = [I_{inv} - \frac{V_g}{Z_o}].\frac{1}{1+\frac{Z_g}{Z_o}}, \tag{3}$$

where the impedance $\frac{Z_g}{Z_o}$ is the ratio of the grid impedance to the inverter output impedance. This impedance ratio, also

called the minor loop gain (T_{ml}), should satisfy the GNC in order for the system to be stable. The stability of the grid-connected inverter system can be assessed based on the GNC using the following equation [23]:

$$P(T_{\mathrm{clm}}) = P(T_{\mathrm{ml}}) - N_{(-1,j0)}P(T_{\mathrm{ml}}), \tag{4}$$

where $P(T_{\mathrm{clm}})$ and $P(T_{\mathrm{ml}})$ are the numbers of the right-hand poles (RHP) of the closed minor loop gain and the minor loop gain, respectively. $N_{(-1,j0)}$ denotes the net sum of anticlockwise encirclements of the critical point $(-1, j0)$ by the set of characteristic loci of the impedance ratio, $T_{\mathrm{ml}} = \frac{Z_{\mathrm{g}}}{Z_{\mathrm{out}}}$. Then, the inverter system is stable only if $P(T_{\mathrm{ml}})$ and $N_{(-1,j0)}(P(T_{\mathrm{ml}}))$ are equal [24], [25].

For simplicity, the impedance-based stability analysis is performed in the dq reference frame [16]. In this case, the matrices of the inverter output impedance ($Z_{\mathrm{o-dq}}(s)$) and grid impedance ($Z_{\mathrm{g-dq}}(s)$) in the dq reference frame are as follows:

$$Z_{\mathrm{o-dq}}(s) = \begin{bmatrix} Z_{\mathrm{odd}}(s) & Z_{\mathrm{odq}}(s) \\ Z_{\mathrm{oqd}}(s) & Z_{\mathrm{oqq}}(s) \end{bmatrix}, \tag{5}$$

$$Z_{\mathrm{g-dq}}(s) = \begin{bmatrix} Z_{\mathrm{gdd}}(s) & Z_{\mathrm{gdq}}(s) \\ Z_{\mathrm{gqd}}(s) & Z_{\mathrm{gqq}}(s) \end{bmatrix} = \begin{bmatrix} R_{\mathrm{g}} + sL_{\mathrm{g}} & -\omega_s L_{\mathrm{g}} \\ \omega_s L_{\mathrm{g}} & R_{\mathrm{g}} + sL_{\mathrm{g}} \end{bmatrix}, \tag{6}$$

where $Z_{\mathrm{g-dq}}(s)$ is the equivalent grid impedance (RL model) in the dq reference frame. ω_s is the system angular frequency measured in rad/s. The cross-coupling impedances $Z_{\mathrm{gdq}}(s)$ and $Z_{\mathrm{gqd}}(s)$ can be neglected due to their small values during inverter operation at the unity power factor [26]. Hence, it is sufficient to perform the stability analysis in the d-axis and q-axis based on the diagonal elements. Additionally, it is worth mentioning that for the RL model of the grid impedance, -$Z_{\mathrm{gdq}}(s)$ and $Z_{\mathrm{gqd}}(s)$ are equal. Therefore, it is sufficient to obtain $Z_{\mathrm{gdd}}(s)$ or $Z_{\mathrm{gqq}}(s)$ [27]. Then, the impedance information can be used for stability analysis purposes.

The minor loop gains of the diagonal elements in the d-axis ($T_{\mathrm{ml-d}}$) and in the q-axis ($T_{\mathrm{ml-q}}$) are:

$$T_{\mathrm{ml-d}} = \frac{Z_{\mathrm{gdd}}}{Z_{\mathrm{odd}}}, \tag{7}$$

$$T_{\mathrm{ml-q}} = \frac{Z_{\mathrm{gqq}}}{Z_{\mathrm{oqq}}}. \tag{8}$$

To compare the stability of the VCC, VMDPC, and LPV-PSC, the impedance-based stability analysis of the three control techniques is investigated in this part, considering the operation in three grid conditions: strong, weak, and very weak grids. In addition, the stability is assessed for all inverters while operating at unity power factor, in which the power reference commands are set as $P_{\mathrm{ref}} = 4$ MW and $Q_{\mathrm{ref}} = 0$ MVar.

The first step to perform the impedance-based stability analysis in the dq reference frame is required to obtain both 1) the output impedance of the inverter in the d-axis (Z_{odd}) and in the q-axis (Z_{oqq}), and 2) the grid impedance in the d-axis (Z_{gdd}) and in the q-axis (Z_{gqq}). While Z_{odd} and Z_{oqq} are calculated analytically, Z_{gdd} and Z_{gqq} can be accurately estimated online by the inverter itself [19], [28], [29].

Fig. 6(a)-(d) present the output impedances of the VCC-OLPC and the VCC-OLPC with the V_{dq} LPF in both the d-axis and q-axis. Based on the Bode plots, on the one hand, it can be seen that the systems are stable in the d-axis as the phase angle differences between Z_{odd} and Z_{gdd} in strong (Z_{g1}), weak (Z_{g2}), and very weak (Z_{g3}) grids are less than 180°. On the other hand, Fig. 6(c) predicts that the VCC-OLPC will be stable only in a strong grid condition. However, the inverter will not be stable if it is required to inject its rated active power without the support of reactive power injection, where the phase angle differences between Z_{odd} and Z_{gdd} in both weak and very weak grids are 242° and 251°, which are greater than the maximum limit of 180° [30].

The predicted (in)stability phenomenon of the VCC in a weak grid is in accordance with the time-domain simulation results shown in Fig. 8(a), where the step change is applied at 0.2 s in the active power references from $P_{\mathrm{ref}} = 2$ MW to $P_{\mathrm{ref}} = 4$ MW and a step change in the reactive power from $Q_{\mathrm{ref}} = 2$ MVar to $Q_{\mathrm{ref}} = 0$ MVar at 0.24 s. The instability of the VCC shows a poor dynamic response in very weak grid conditions, resulting in an undamped oscillatory response. Additionally, the VCC controller fails to regulate the PCC active power to its desired reference after 0.24 s, as shown in Fig. 8(d).

In addition, adopting the second-order LPF, presented in (1), in the control loop increases the stability margin of the VCC. For example, the inverter can now inject its rated active power without the need to inject reactive power in weak grid conditions. Now, the phase angle difference is 162°, less than the maximum limit of 180°. Fig. 6(d) also shows that adding the LPF improves the stability margin in both strong and very weak grids. However, the operation in a weak grid is still unstable, as the phase angle difference between the Z_{oqq} and Z_{g3} is 215° at 73 Hz.

The corresponding Nyquist diagrams based on (7) for VCC equipped with the OLPC without and with the LPF are shown in Fig. 6(e)-(h). For the VCC-OLPC without the LPF, it is evident in Fig. 6(e) that the characteristic loci in the d-axis do not encircle the critical point (−1, j0) in the cases of SCR = 16.8, 3.21, and 1.21. Fig. 6(g) predicts the unstable operation of the system in both weak and very weak grids as the root loci encircle the critical point (−1, j0), confirming the previous findings obtained from Bode plots as presented in Fig. 6(c). However, the Nyquist diagrams in the q-axis based on (8) for VCC equipped with the OLPC with the LPF indicate that only the characteristic loci encircle the critical point (−1, j0) in case of very weak grid conditions.

Fig. 7 presents a similar analysis applied to the grid-connected inverters equipped with the VMDPC and LPV-PSC. For both controllers, the output impedances are obtained for the same operation point in which the power reference commands are set as $P_{\mathrm{ref}} = 4$ MW and $Q_{\mathrm{ref}} = 0$ MVar.

It is evident from the Bode plot that for the q axis of the VMDPC, as shown in Fig. 7(c), that the system stability

margin is decreased under weak grid conditions. These results are confirmed by the corresponding Nyquist diagrams presented in Fig. 7(g), where the root loci are approaching the critical point (−1, j0) in a very weak grid with an SCR = 1.21.

Fig. 6(g) predicts the unstable operation of the system in both weak and very weak grid conditions, since the root loci encircle the critical point (−1, j0), confirming the previous findings, including the Bode plot results presented Fig. 6(c). These findings also will be verified by the time-domain simulation results as shown in Fig. 9 and in Fig. 14 for strong and weak grid conditions.

Lastly, the analysis of the PLL-less LPV-PSC is presented in Fig. 7. It can be observed clearly from the Bode plot of the minor loops in the d-axis and q-axis, shown in Fig. 7(b) and Fig. 7(d), respectively, that the phase margins are much higher than those of the VCC and VMDPC. For example, the phase margins of the VMDPC and the LPV-PSC in the q axis during the operation in a very weak grid are 39° and 51°, respectively.

IV. TIME-DOMAIN RESULTS

To further assess the performance of the three controllers, MATLAB/Simulink is used. The block diagrams of the simulated VCC, VMDPC, and LPV-PSC control systems are shown in Fig. 2, Fig. 3, and Fig. 4, respectively. The parameters of the three control systems used in the simulation are listed in Table 1.

As different approaches can be used to generate current reference commands, the effects of three different current reference generation methods for the VCC are initially studied in strong and weak grids. Then, the performance of the VCC, VMDPC, and LPV-PSC controllers is evaluated for operating in strong, weak and very weak grids. In each operating condition, five different scenarios are evaluated: 1) step change of active and reactive power, 2) frequency jump, 3) phase jump, 4) three-phase permanent voltage sag in the grid voltage, and 5) three-phase fault at the PCC for a duration of 100 ms.

A. EFFECTS OF THREE CURRENT REFERENCE GENERATION METHODS FOR THE VCC

Fig. 8 compares the time-domain response of the VCC for the different approaches to generate $i_{\mathrm{dq,\ ref}}$ in strong and weak grid conditions. First, the response of the VCC when $i_{\mathrm{d,\ ref}}$ and $i_{\mathrm{q,\ ref}}$ are directly specified to the inner current controller (ICC), without using the OLPC, is also shown in the same figure, and this case study is donated by the VCC-ICC. The second and third cases correspond to the VCC when the $i_{\mathrm{dq,\ ref}}$ is generated by the outer loop using non-filtered and filtered V_{d} and V_{q}, denoted by "VCC-OLPC" and "VCC-OLPC with filter", respectively. Furthermore, the response of the VCC when $i_{\mathrm{d,\ ref}}$ and $i_{\mathrm{q,\ ref}}$ are directly specified to the inner current controller (ICC), without using the OLPC, is also shown in the same figure, and this case study is donated by the VCC-ICC.

The presented results in Fig. 8 consider three different grid conditions, i.e., a strong grid with a short circuit ratio (SCR) equal to 16.8, a weak grid with an SCR equal to 3.21, and a very weak grid with an SCR equal to 1.21. For a strong grid scenario shown in Fig. 8(a)-(c), it can be observed that the measured power at the PCC (i.e., P and Q) follows the reference power command with zero steady-state error only for the case of VCC-OLPC with filter. On the contrary, the VCC-OLPC produces steady-state oscillations in the injected power to the grid, and the VCC-ICC injects slightly higher power than the desired power commands. The differences between the VCC-ICC, VCC-OLPC, and VCC-OLPC with filter become clearer under a weak grid shown in Fig. 8(d)-(f) and a very weak grid shown in Fig. 8(g)-(i). In a weak grid scenario, in contrast to both the VCC-ICC and VCC-OLPC, only VCC-OLPC with filter is able to track the desired active and reactive power reference commands with zero steady-state errors, as shown in Fig. 8(e) and Fig. 8(f), respectively.

The effects of these three approaches followed to generate $i_{\mathrm{d,\ ref}}$ and $i_{\mathrm{q,\ ref}}$ become very clear in a very weak grid conditions. First, the VCC-ICC fails to operate, where the controller is unstable even when the inverter injects half of its rated reactive power ($Q_{ref} = 1.5$ MVar) to support the grid. However, the OLPC and VCC-OLPC with filter maintain stable operation as long as the inverter supports the grid with reactive power. For example, the operation of these two control approaches becomes unstable only at $t = 0.24$ s after the reactive power reference command is set to zero, e.g., $Q_{ref} = 0$ MVar.

For the comparison study in the time-domain with the VMDPC and LPV-PSC presented in the rest of this section, the VCC-OLPC with filter is used. Hence, for simplicity, the abbreviation "VCC" is used instead of "VCC-OLPC with filter".

B. PERFORMANCE EVALUATION OF VCC,VMDPC, AND LPV-PSC IN STRONG GRID

This part reports the performance of the three control systems in a strong grid with an SCR = 16.8. The obtained results from the five testing conditions are presented below.

1) RESPONSE TO STEP CHANGE IN POWER REFERENCES

The step changes in active and reactive power references are applied to assess the dynamic responses of the three controllers in the time-domain. First, the three control systems operate in steady-state conditions, where the active and reactive power references are set to $P_{\mathrm{ref}} = 2$ MW and $Q_{\mathrm{ref}} = 1.5$ MVar, respectively. Then, a step change of the active power to $P_{\mathrm{ref}} = 4$MW is applied at $t = 3$ s. Finally, a step change of the reactive power Q_{ref} to 0 MVar is applied at $t = 5$ s. Fig. 9(a), (d), and (g) shows the inverter output current when the VCC, VMDPC, and LPV-PSC are in service, respectively.

Differently from the VCC and VMDPC, it should be noted that the measured active and reactive power of the LPV-PSC shown in Fig. 9(b) are the terminal power instead of the PCC power, where the PCC power is slightly lower than the desired

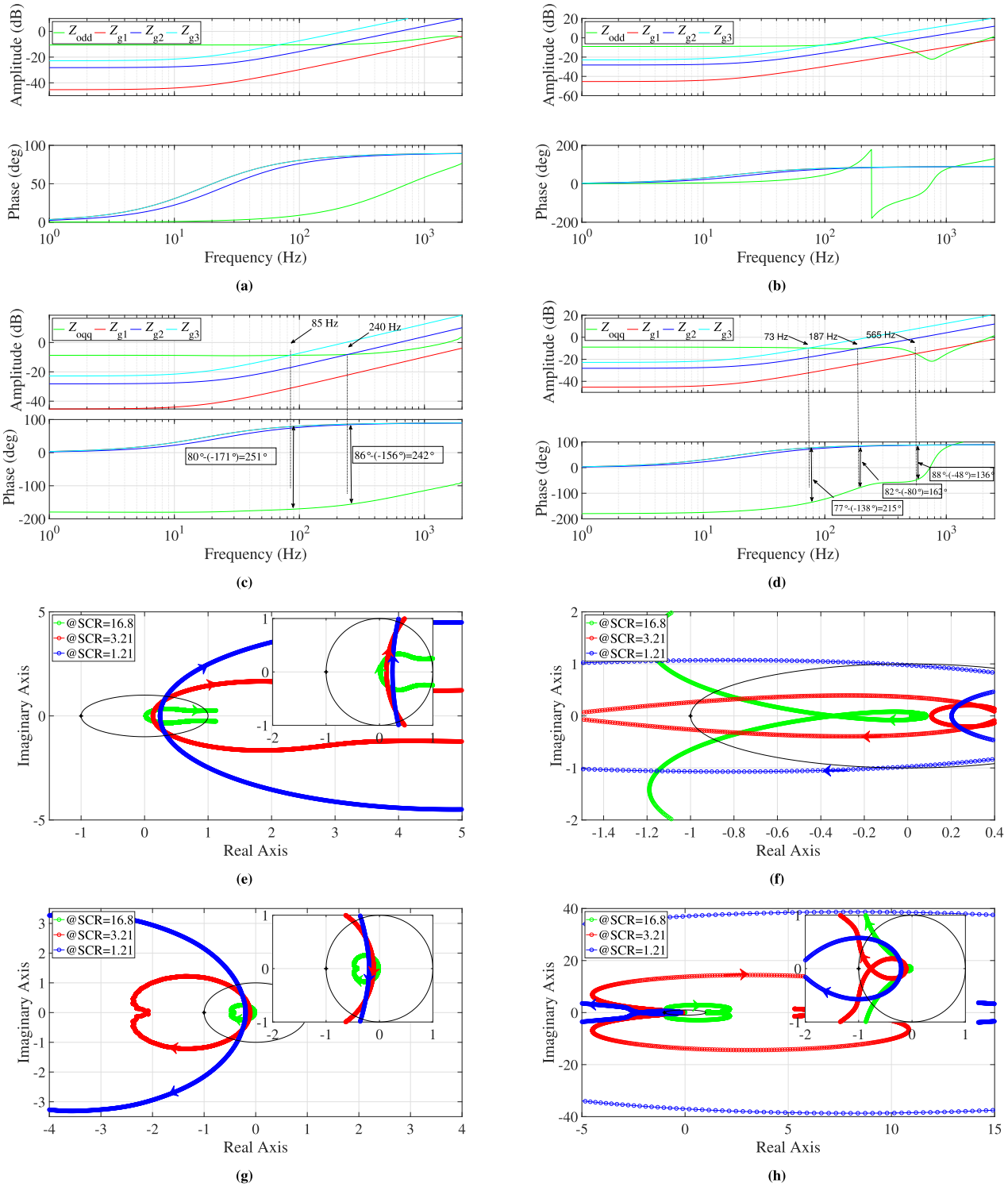

FIGURE 6. **Frequency-domain performance evaluation for the PLL-based VCC inverter when injeting full active power and 0 Var; where the VCC-OLPC without filter (a),(c),(e) and (g) and VCC-OLPC with filter (b),(d),(f) and (h) operating in three grid conditions (Strong grid (Z_{g1}, weak grid Z_{g2}, very weak grid Z_{g1}): (a) and (b) the output impedances of the inverters and the grid impedances in the d-axis; (c) and (d) the output impedances of the inverters and the grid impedances in the q-axis; (e) and (f) stability assessment at d-axis based on the Generalized Nyquist Criterion; and (g) and (h) stability assessment at q-axis based on the Generalized Nyquist Criterion.**

references due to the power consumption caused by the L filter. Therefore, as for the results presented in this article, the terminal active and reactive powers of the LPV-PSC are used because the LPV-PSC control regulates the terminal

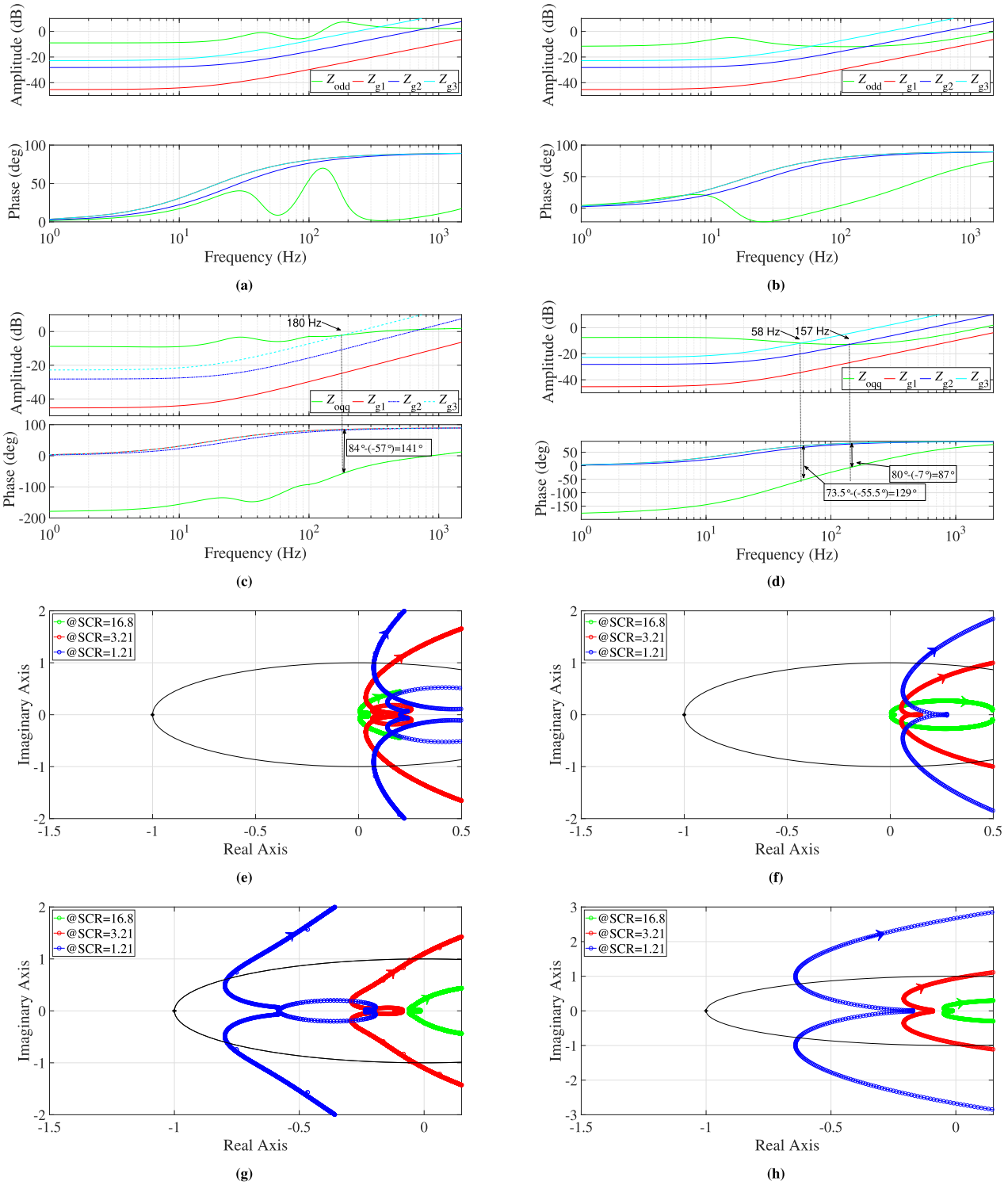

FIGURE 7. Frequency-domain performance evaluation for the VMDPC (a),(c),(e) and (g) and LPV-PSC (b),(d),(f) and (h) operating in three grid conditions (Strong grid (Z_{g1}, weak grid Z_{g2}, very weak grid Z_{g1}): (a) and (b) the output impedances of the inverters and the grid impedances in the d-axis; (c) and (d) the output impedances of the inverters and the grid impedances in the q-axis; (e) and (f) stability assessment at d-axis based on the Generalized Nyquist Criterion; and (g) and (h) stability assessment at q-axis based on the Generalized Nyquist Criterion.

power (e.g., before the L-filter) instead of the PCC power (e,g, after the L-filter).

Fig. 9(b) shows that the three controllers are able to track the power reference commands with zero steady-state

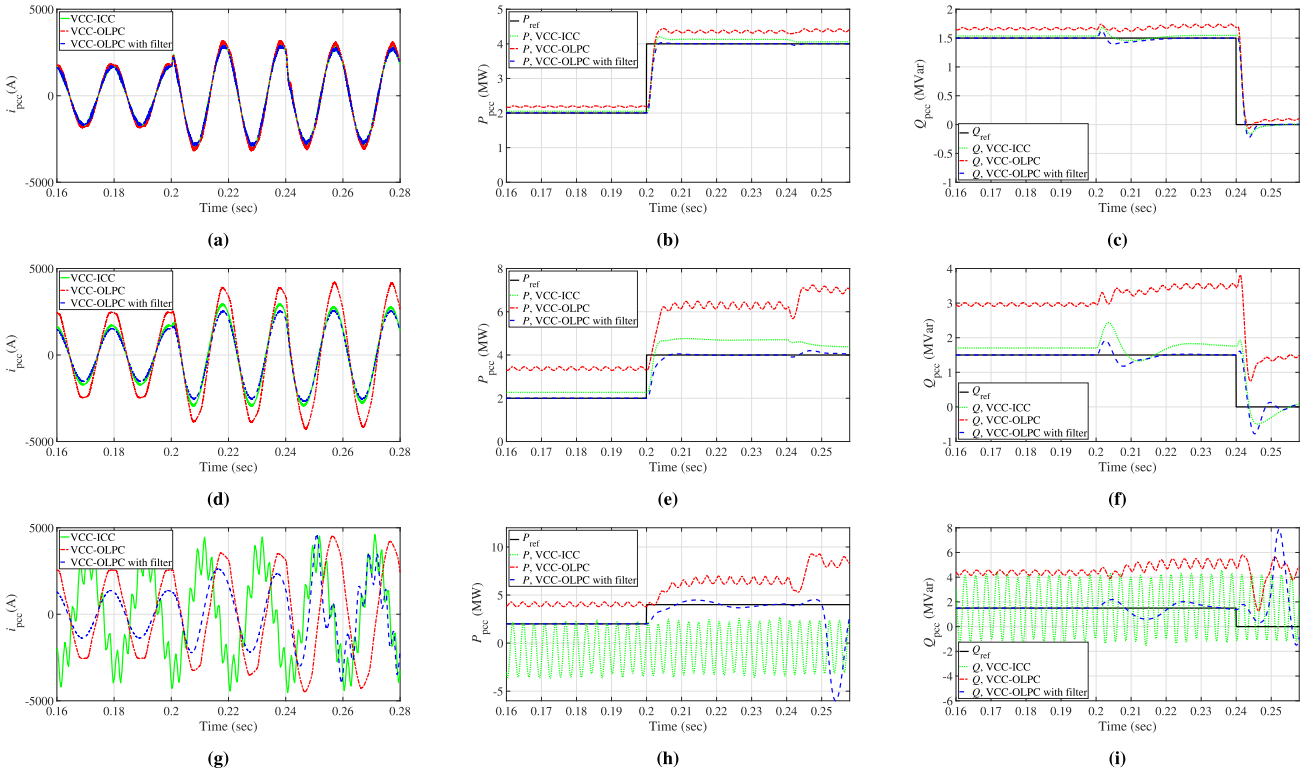

FIGURE 8. Performance of PLL-based (VCC) inverters considering three different method for generating the current reference in: (a)-(c) a strong grid with SCR = 16.8,(d)-(f) a weak grid with SCR = 3.21, (g)-(i) a very weak grid with SCR = 1.21.

error. Compared to their VMDPC counterparts, the dynamic responses of the VCC and LPV-PSC are faster and more damped responses under step changes in the active and reactive power reference commands. However, the VMDPC shows a poor dynamic response. It requires around $t = 1.5$ s to reach the steady-state. Fig. 9(c) presents the estimated frequency in the control loops of the VCC and LPV-PSC. The internal frequency generated in the control loop of the LPV-PSC is identical to the grid frequency in steady-state operation. However, compared to the estimated frequency by the VCC, it has a higher amplitude after the transient events at 3 and 5 s.

2) FREQUENCY JUMP

To evaluate the performance of the three controllers during abnormal conditions, different frequency jumps in the grid voltage source are applied. Then, the responses of the VCC, VMDPC, and LPV-PSC control systems are observed and compared. During this test, the active and reactive power reference commands are set as $P_{\text{ref}} = 4$ MW and $Q_{\text{ref}} = 1.5$ MVar, respectively.

Initially, the frequency of the grid voltage source is 50 Hz. Then, this grid frequency is reduced by 0.05 Hz each time at $t = 3$ s. The reported results are shown in Fig. 10. Overall, it can be seen that the VCC and LPV-PSC controllers are shown to be robust against the frequency jump, and they track the grid frequency with zero overshoot as shown in Fig. 10(c), (f) and (i) [15]. Furthermore, there are no overshoots in the injected current and power in response to the slight drop in frequency, as shown in Fig. 10(a), (d), (f), (b), (d), and (h), respectively.

Compared to the VCC, the PLL-less LPV-PSC has a faster response after the frequency excursion events. Notably, the injected active power and reactive power by the LPV-PSC are slightly drifted from the desired references. However, Fig. 10 shows that the VMDPC is less stable and has a large transient during the frequency jump at $t = 3$ s. For instance, it can be seen that the VMDPC has a settling time of a few seconds to regulate the PCC current and the injected power to the desired power references before the frequency decrease events during the frequency drop from 50 Hz to 49.5 Hz, as shown in Fig. 10(a) and Fig. 10(b), respectively.

To mitigate the negative impacts of frequency step changes on the transients of the VCC and the DPC and on the steady-state power errors of the LPV-PSC, an adaptive frequency mechanism may be adopted

3) PHASE ANGLE JUMP

Similar to the previous case study, the active and reactive power reference commands for the three controllers are kept constant at $P_{\text{ref}} = 4$ MW and $Q_{ref} = 1.5$ MVar. Then, two different case studies that represent frequency jumps with 15°

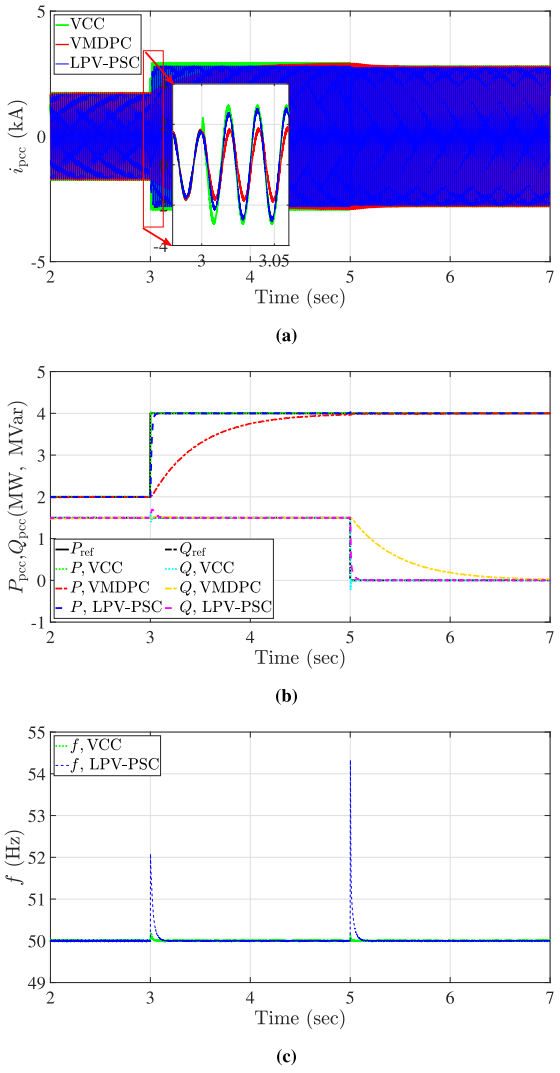

FIGURE 9. Step response of the PLL-based (VCC) and PLL-less (VMDPC, LPV-PSC) grid-following inverters in a strong grid with SCR = 16.8 upon changes in the active and reactive power references: (a) PCC current, (b) real and reactive powers, and (c) frequency.

and 45° in the grid voltage source are investigated. In each case study, the frequency jump event is applied at $t = 3$ s to the three phases of the grid voltage source.

Fig. 11 shows the dynamic response of the three controllers in a strong grid case. Overall, the PLL-based VCC, the PLL-less VMDPC, and the PLL-less LPV-PSC remain stable after the phase jump. Again, the response of the VCC and the LPV-PSC to the two events of the phase jumps outperform that of the VMDPC in terms of faster response and regulation of the active and reactive power to their desired references. As shown in Fig. 11, the VMDPC method requires a longer settling time to reach the steady-state operation before applying the disturbance.

It is worth mentioning that the presented results in this article, during the comparison of the three controllers, do not consider the implementation of current limiters in the control loops of these controllers since the main goal is to test the performance of these controllers for abnormal operating conditions. However, it is necessary to limit the output current of these inverters in practical applications due to safety concerns.

4) GRID VOLTAGE SAG

Fig. 12(a), (b), and (c) shows the system responses under a permanent grid voltage sag with an amplitude of 20%V_g. Another case study where the grid voltage is decreased to 50% is shown in Fig. 12(d), (e), and (f). Considering the active and reactive power regulations, it is evident from Fig. 12(b) and (e) and Fig. 12(c) and (f) that the VCC and LPV-PSC are stable against the two voltage sag events. Furthermore, the LPV-PSC performance proves to be the most robust controller, since it has almost no overshoot in the injected current to the grid during the events of phase jumps in a strong grid condition, as shown in Fig. 12(a) and Fig. 12(d).

5) PCC BALANCED FAULT

The responses of the VCC, VMDPC, and LPV-PSC inverters are tested in this section considering three-phase symmetrical faults in the PCC. Initially, the three inverters regulate the injected power to the desired references, $P_{\text{ref}} = 4$ MW and $Q_{ref} = 2$ MVar. Then, three-phase faults in the PCC are applied at $t = 3$ s for a time duration of $t = 0.1$ s. The applied faults are tested in three different values for the fault resistances (R_{f1}). For example, for the first fault shown in Fig. 13, the R_{f1} is set to 5 mΩ, whereas R_{f1} is set to 10 mΩ and 20 mΩ for the second and third faults, respectively.

Fig. 13(a), (d), and (g) show the output current of the inverters. In general, it can be seen that the fault currents increase for small values of R_{f}. The VMDPC fails to stay synchronized with the grid frequency for transients at $t = 3$ s, $t = 3.1$ s, and the time interval between the occurrence and clearance of a fault. On the other hand, the VCC and the LPV-PSC are able to be kept synchronized with the grid frequency, and they maintain the amplitudes of the injected real and reactive power to the grid during the fault events, which are much smaller than the injected powers by the VMDPC.

C. PERFORMANCE OF VCC,VMDPC, AND LPV-PSC IN WEAK GRIDS

Similar to the tested conditions applied for a strong grid case, the performance of the three control modes is evaluated here in a weak grid with SCR = 3.21 case. The parameters of the three controllers are kept identical to those used in the strong grid case, as listed in Table 1. It is worth mentioning that throughout the comparison study the output filter parameters (R_f, L_f) are kept constant. While the performance of the three control strategies are good in strong grid conditions, the parameters of the output filter must be redesigned for weak and very weak grid conditions. A detailed comparison considering the operation of the PLL-based (VCC) and PLL-less (VMDPC, LPV-PSC) GFLIs in weak grid conditions is presented below.

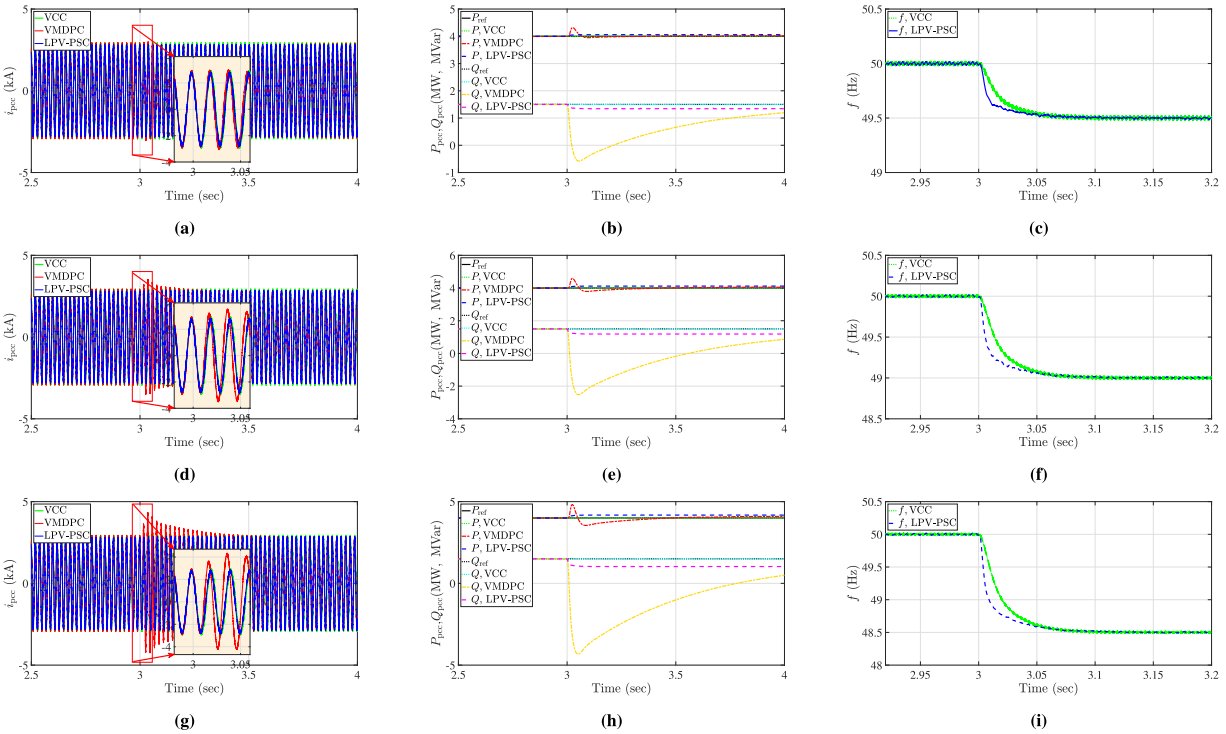

FIGURE 10. Response of the PLL-based (VCC) and PLL-less (VMDPC, LPV-PSC) grid-following inverters in a strong grid with SCR = 16.8 under frequency jumps drop of the grid voltage source at 3 sec from 50 Hz to : (a), (b), (c) 49.5 Hz; (d), (e), (f) 49 Hz; (g), (h), (i) 48.5 Hz.

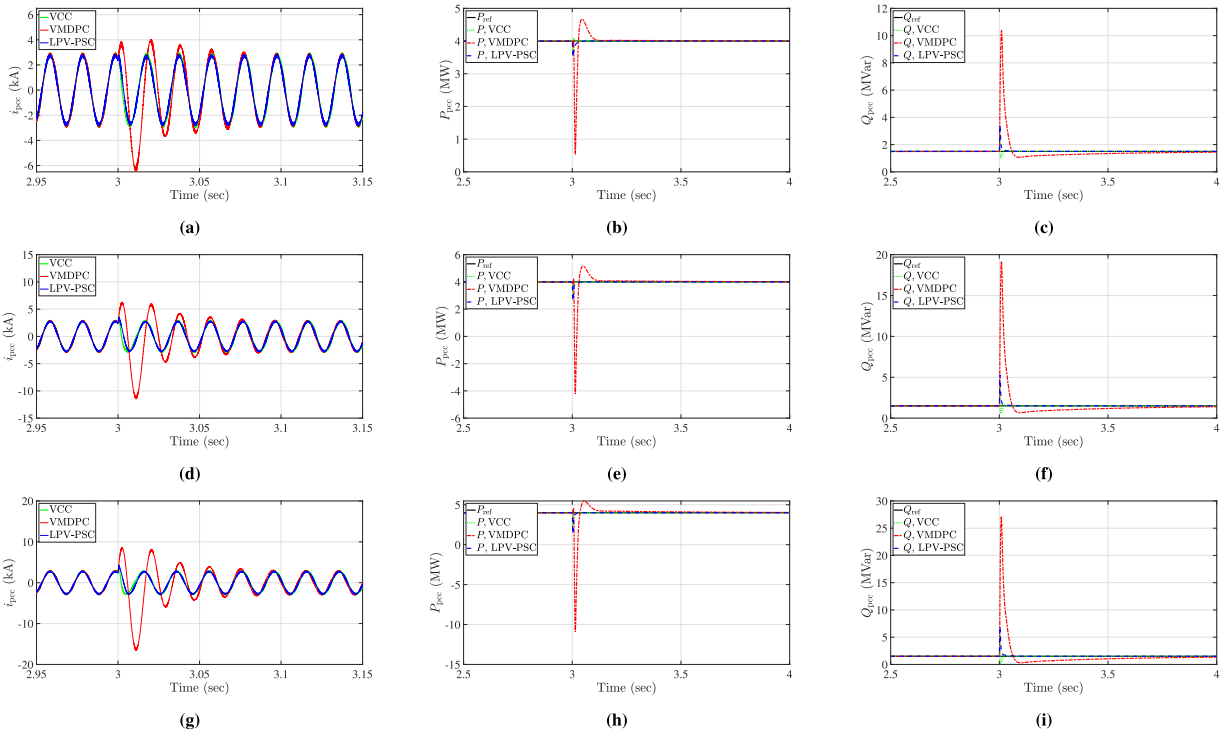

FIGURE 11. Response of the PLL-based (VCC) and PLL-less (DPC, LPV-PSC) grid-following inverters in a strong grid with SCR = 16.8 under phase jumps in the grid voltage source: (a)-(c) 15° phase jump; (d)-(f) 30° phase jump; (g)-(i) 45° phase jump.

1) RESPONSE TO STEP CHANGE IN POWER REFERENCES

The time-domain responses are evaluated for a step change of the active and reactive power references in both a weak grid and a very weak grid. Initially, the power reference commands of the three control systems are set as $P_{\text{ref}} = 2$ MW and $Q_{\text{ref}} = 1.5$ MVar, respectively. Then, the step change to

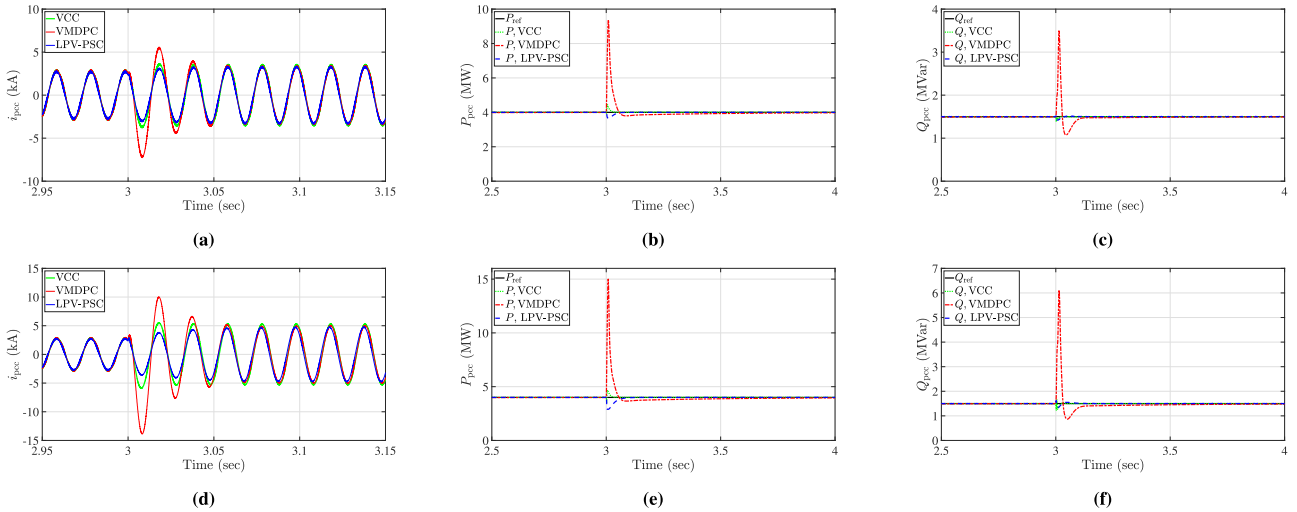

FIGURE 12. Response of the PLL-based (VCC) and PLL-less (VMDPC, LPV-PSC) grid-following inverters in a strong grid with SCR = 16.8 under permanent voltage in the grid voltage source: (a)-(c) 20%V_g; (d)-(f) 50%V_g.

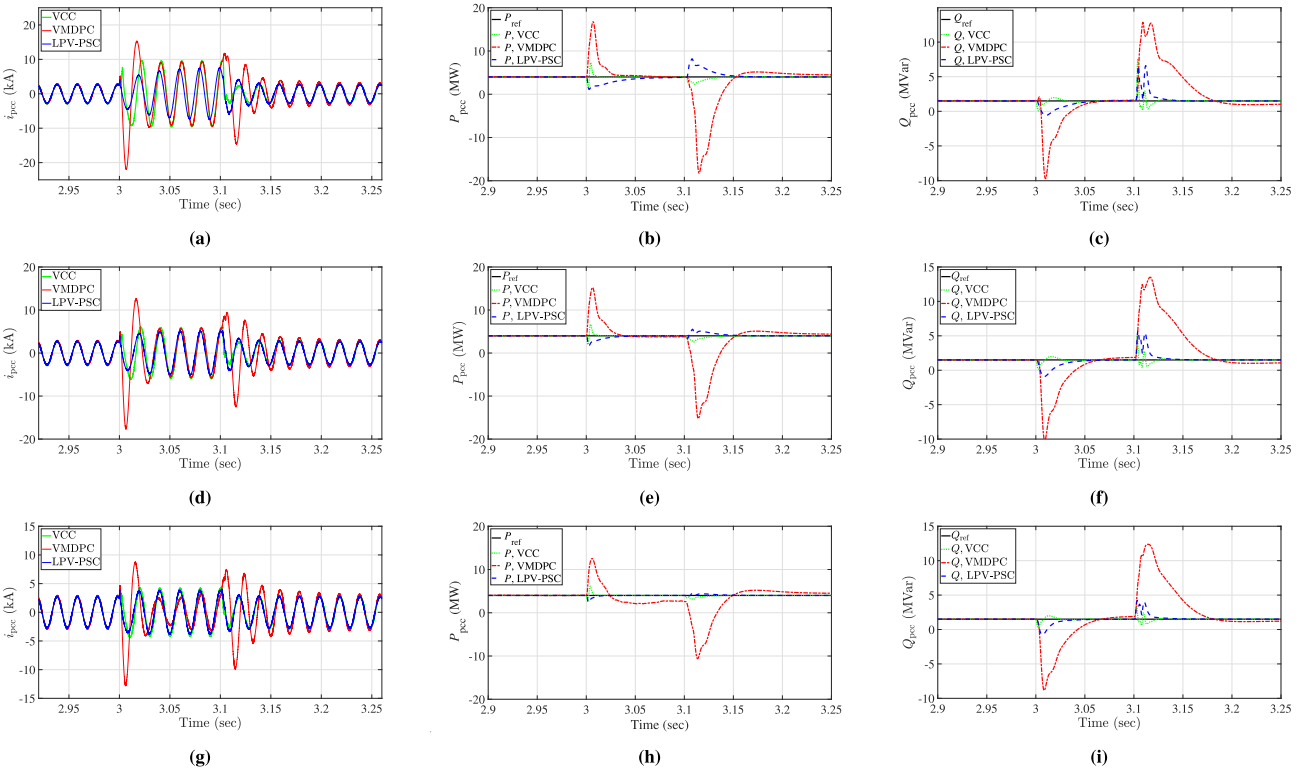

FIGURE 13. Output current and powers a response of the PLL-based (VCC) and PLL-less (VMDPC, LPV-PSC) grid-following inverters in a strong grid with SCR = 16.8 under 3-ph fault line to ground at the PCC for three different values for the fault resistance at: (a)-(c) $R_{f1} = 0.005\ \Omega$; (d)-(f) $R_{f1} = 0.01\ \Omega$; (g)-(i) $R_{f1} = 0.02\ \Omega$.

$P_{\text{ref}} = 4$ MW and $Q_{\text{ref}} = 0$ MVar are applied at $t = 3$ s and $t = 5$ s, respectively.

Fig. 14(a), (b), and (c) show the inverters output current, power, and frequency in a weak grid, respectively. First, the VCC and LPV-PSC maintain good performance without overshoot during the transients, where they are able to regulate the real and reactive power to their desired references. Besides its slow response, the VMDPC controller is less robust against changes in the power references, and its output power oscillates after changing the power reference commands. Furthermore, unlike the LPV-PSC, the VCC and VMDPC are required to generate a certain amount of reactive power in order to inject the full rated active power to (very) weak grids [11].

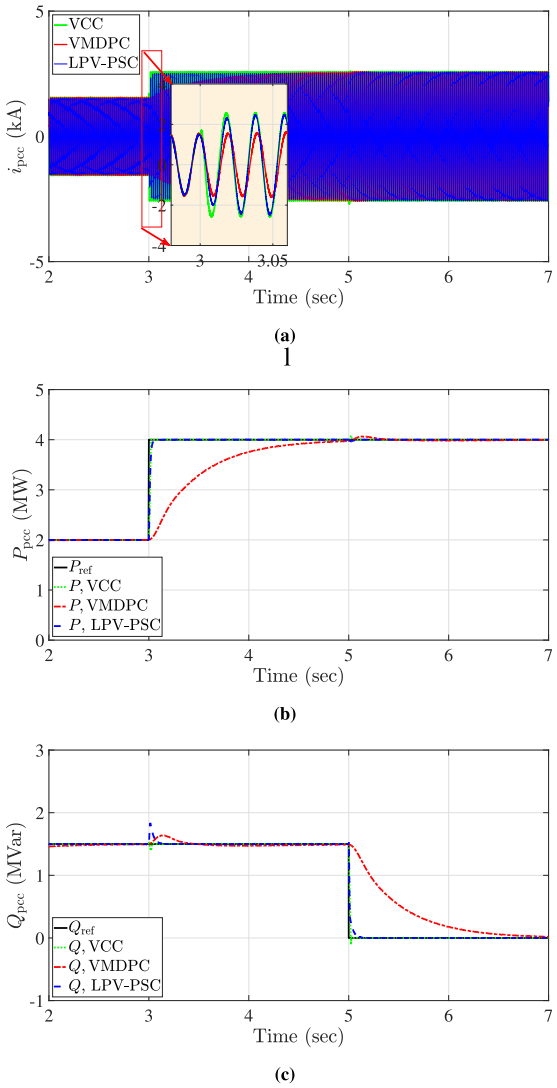

FIGURE 14. Step response of the PLL-based (VCC) and PLLless (VMDPC, LPV-PSC) grid-following inverters in a weak grid with SCR = 3.21 upon changes in the active and reactive power references: (a) PCC current, (b) real and reactive powers, and (c) frequency.

2) FREQUENCY JUMP

Fig. 14 shows the dynamic response of the three controllers in a weak grid (SCR = 3.21), where three different frequency jumps in the grid voltage source are applied at $t = 3$ s. It can be observed that the VCC is the most robust to the frequency change. Then, the LPV-PSC control system has good performance. In contrast, there is a slight steady-state increase in the inverter output active power and a slight steady-state decrease in the inverter output reactive power as shown in Fig. 14(b), (e), and (h) that are associated with the frequency decrease to 49.5 Hz, 94.0 Hz, and 48.5 Hz, respectively. Similarly to operation in a strong grid, the LPV-PSC is faster to capture the changes in grid frequency than the VCC, as presented in Fig. 14 (c), (f), and (i).

In contrast to the stable operation of the VCC and LPV-PSC, the performance of the inverter equipped with the VMDPC is significantly affected by the frequency jump events. For instance, the VMDPC produces oscillations in the output current that last more than one second for a frequency excursion below 49 Hz, as presented in Fig. 14(g). Another example is the sudden drop of the injected reactive power. It jumps from $Q = 1.5$ MVar to around $Q = -3$ MVar, when the grid frequency is decreased from 50 Hz to 48.5 Hz, as shown in Fig. 14(h). The absorption of such an amount of reactive power could threaten the system stability in multi-connected inverters equipped with the VMDPC control technique, since it may lead to cascade failures in the system due to grid voltage dips at the PCC that correspond to frequency changes.

3) PHASE-ANGLE JUMP

This study investigates three abnormal conditions. At each condition, a different value of the phase angle jump occurs in the grid voltage source. In this article, three different values for the phase angle jump are simulated, 15°, 30°, and 45°.

Fig. 16 shows the three-phase currents, active and reactive powers of the inverters. In summary, the VCC and LPV-PSC show to remain very stable under the three different phase jump events. There are almost no overshoots, and the controllers remain synchronized with the grid frequency, as shown in Fig. 16(a) and (d). In contrast, the VMDPC is less robust to phase jumps. For instance, the inverter output active power is reduced sharply from $P = 4$ MW to $P = -5$ MW during the phase angle jump of 45°. Similarly, the output reactive power is very sensitive to the phase angle jump, as it increases from $Q = 1.5$ MVar to $Q = 5.5$ MVar for the same event of the phase angle jump.

4) GRID VOLTAGE SAG

Fig. 17(a)-(c) and Fig. 17(d)-(f) compare the responses of the PLL-based (VCC) and PLL-less (VMDPC, LPV-PSC) GFLIs in a weak grid with SCR = 3.21 under permanent voltage sag in the grid voltage source with amplitude equal to 20% V_g and 50% V_g, respectively. It can be observed that the VCC and LPV-PSC outperform the VMDPC in terms of overshoot in the active and reactive powers at the moment of voltage sag occurrence at $t = 3$ s. For instance, while the active power injected by the VMDPC increases suddenly from $P = 4$ MW to $P = 9.5$ MW during the grid voltage sag with the amplitude of 50%V_g, as shown in Fig. 17(e), the injected power by the VCC and LPV-PSC vary by around $P = 1$ MW in correspondence to the same grid voltage sag event. Similar observations are shown in the inverter output reactive power response for the two grid voltage sag events, as shown in Fig. 17(c) and (f).

Notably, considering both grid voltage sag events, the LPV-PSC shows to have no overshoot in the inverter output current, as presented in Fig. 17(a) and (d). The same observations are also observed in the strong grid case as shown earlier in Fig. 12(a) and (d).

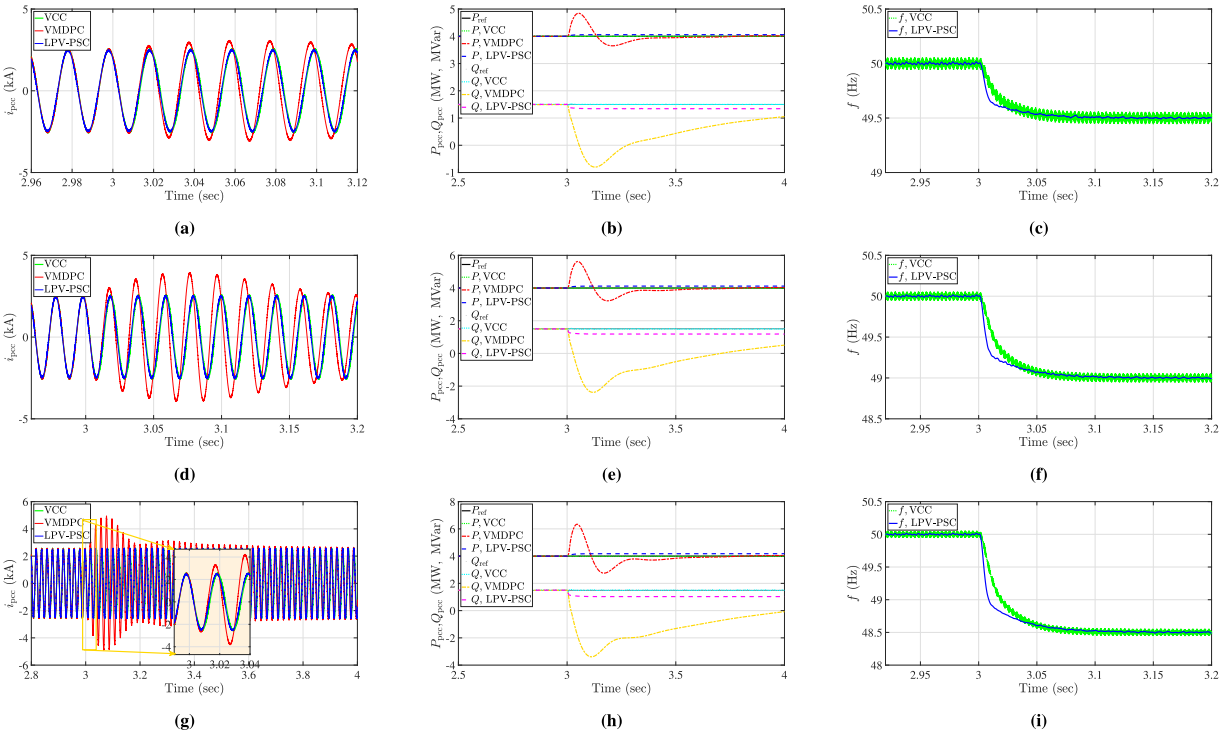

FIGURE 15. Response of the PLL-based (VCC) and PLL-less (VMDPC, LPV) grid-following inverters in a weak grid with SCR = 3.21 under frequency jumps of the grid voltage source from 50 Hz to : (a), (b), (c) 49.5 Hz; (d), (e), (f) 49.0 Hz; (g), (h), (i) 48.5 Hz.

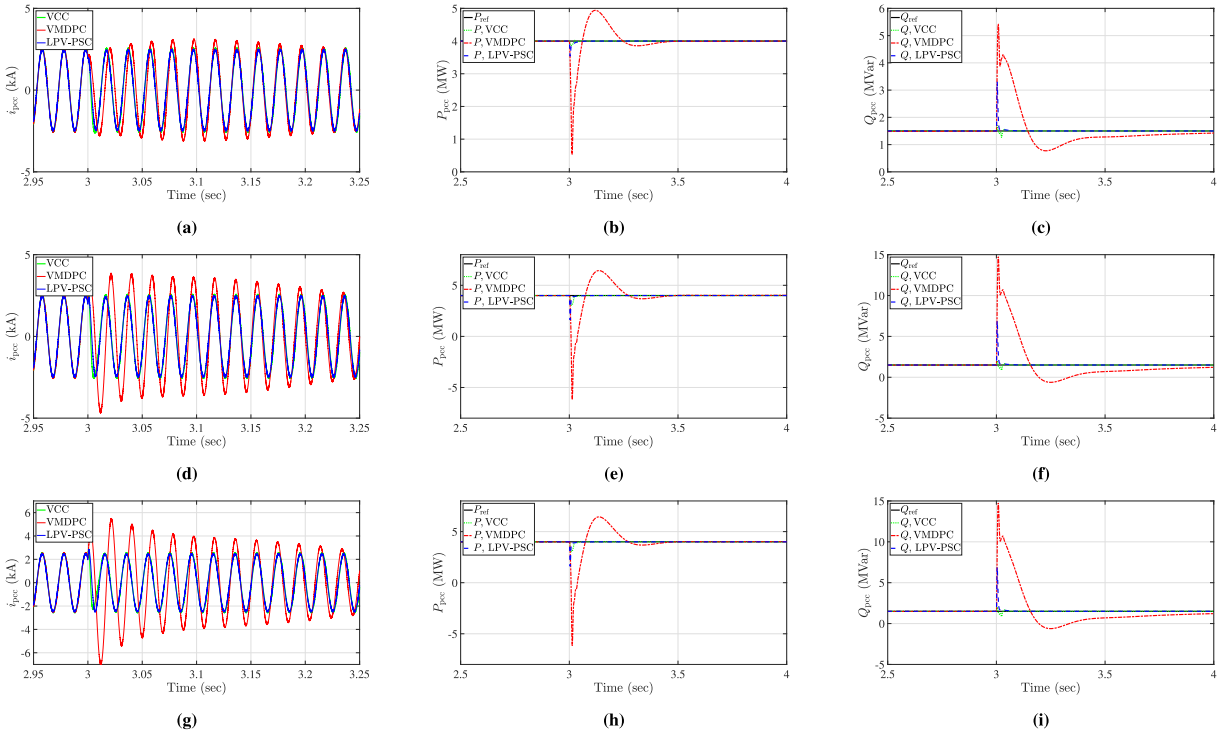

FIGURE 16. Response of the PLL-based (VCC) and PLL-less (VMDPC, LPV-PSC) GFLIs in a weak grid with SCR = 3.21 under phase jumps in the grid voltage source from 50 Hz: (a)-(c) 15 degree; (d)-(f) 30 degree.; (g)-(i) 45 degree.

5) PCC BALANCED FAULT

imilar to the fault test conditions at the PCC in a strong grid case, the same test conditions are applied at the PCC for a weak grid, where the three-phase-to-ground fault resistances are $R_{f1} = 0.001\ \Omega$ $R_{f1} = 0.01\ \Omega$, and $R_{f1} = 0.02\ \Omega$.

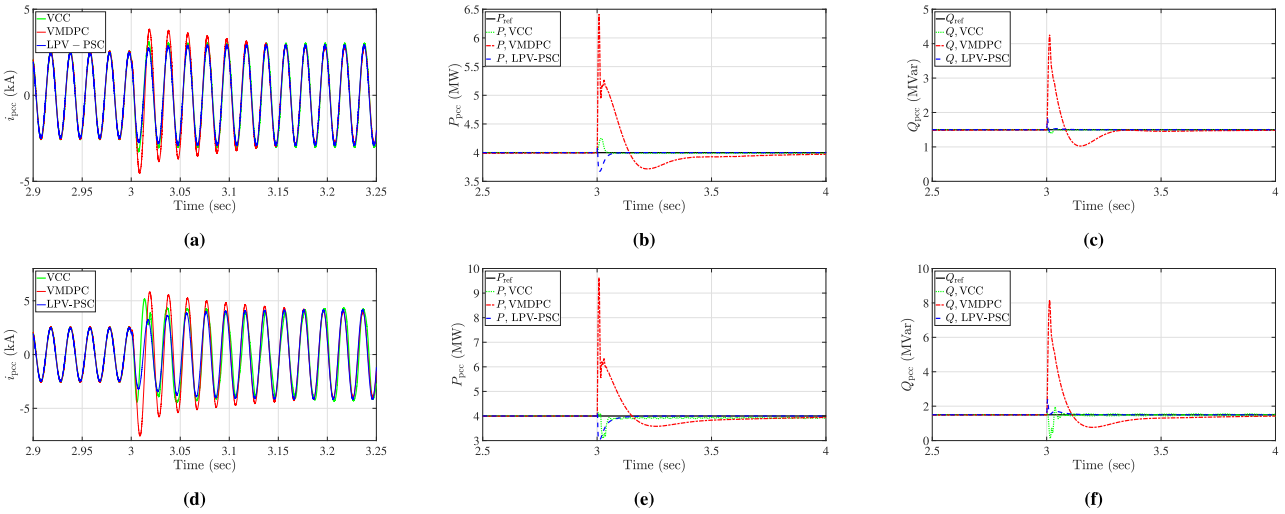

FIGURE 17. Response of the PLL-based (VCC) and PLL-less (VMDPC, LPV-PSC) GFLI in a weak grid with SCR = 3.21 under permanent voltage sag in the grid voltage source: (a)-(c) 20%V_g; (d)-(f) 50%V_g.

Fig. 18(a)-(i) shows the controllers' responses when the faults are applied for the time duration of $t = 100$ ms starting from $t = 3$ s to $t = 3.1$ s. It can be noticed that both the VCC and LPV-PSC achieve better transient responses than the VMDPC. Moreover, the LPV-PSC outperforms the VCC in terms of the amplitude of the produced current during the faults. In contrast to the VCC and LPV-PSC, the frequency of generated current by the VMDPC is drifted during the fault events. Therefore, it requires a longer time to re-synchronize with the grid frequency. For example, the VMDPC needs around $t = 0.4$ s to fully re-synchronize after the faults clearance at $t = 3.1$ s.

Another remarkable observation is the significant peaks of the injected active and reactive power by the LPV-PSC during the fault clearance at $t = 3.1$ s.

D. PERFORMANCE OF VCC,VMDPC, AND LPV-PSC IN VERY WEAK GRIDS

Fig. 19 compares the three controllers in a very weak grid condition (SCR = 1.21). Fig. 19(a), (b), and (c) present the inverters output current active power, and reactive power in a very weak grid, respectively. It can be seen that only the LPV-PSC performs well during the step change in both the active and reactive power reference commands. On the contrary, the VCC fails completely for $t \geq 5$ s to regulate the active power to its desired references. This behaviour agrees with our previous findings in [31]. Although it regulates the active and reactive power to their references for $t \geq 5$ s better than the VCC, the VMDPC shows a poor dynamic response. For instance, the change in the active power reference at $t = 5$ s produces oscillations in the reactive power, as shown in Fig. 19(b) and Fig. 19(c). This indicates the strong coupling between the active and reactive power that hinders the accurate operation of the VMDPC in very weak grids for the same control parameters listed in Table 1 that are designed based on performance trade-offs in maintaining fast response in a strong grid and stable operation in a weak grid.

Furthermore, both the VCC and the LPV-PSC perform well under power reference changes, frequency jump, phase jump, and fault tests. For example, contrary to the VMDPC, the VCC and the LPV-PSC maintain a stable operation after a few fundamental cycles after the fault clearance at 3.1 s. In contrast, even with the reactive power support, the VCC cannot maintain the operation under the permanent voltage sag. This is explained by the network capacity (SCR), which is decreased after applying the voltage sag. In contrast, the VMDPC has poor dynamic performance, and it requires longer time to reach steady-state operation. Furthermore, compared with its performance under weak grid conditions, the VMDPC is less robust in a very weak grid.

V. SUMMARY OF THE COMPARISON RESULTS

Table. 2 summarizes the comparison between the PLL-based (i.e., the VCC) and PLL-less (i.e., the VMDPC and LPV-PSC) control methods used to control GFLIs. Overall, the following remarkable points are concluded.

A. VCC, VMDPC, AND LPV-PSC IN STRONG GRID CONDITION

The performance of the VCC and LPV-PSC outperform the VMDPC. Further clarifications are as follows.

1) Control of active and reactive power: The three controllers allow full control of both the active and reactive power independently in strong grid conditions. However, there are some remarks on the performance of these controllers. On the one hand, the VCC and LPV-PSC have very good dynamic responses since the two controllers are able to provide fast and accurate tracking of the changes of the active and reactive power reference commands. On the other hand,

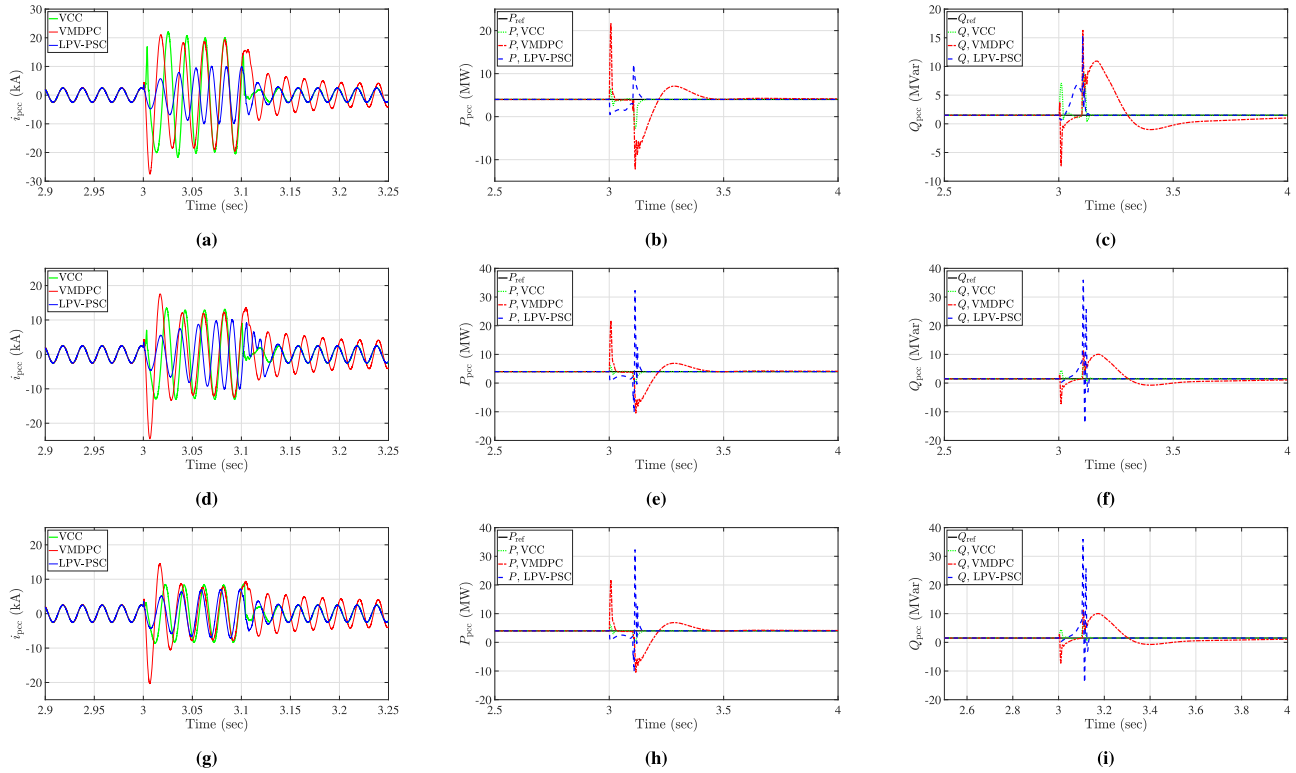

FIGURE 18. Performance of the GFLIs in a weak grid with SCR = 3.21 under 3-ph fault to ground at the PCC for two different values for the fault resistance (R_f) : (a)-(c) $R_{f1} = 0.005\ \Omega$; (d)-(f) $R_{f1} = 0.01\ \Omega$; (g)-(i) $R_{f1} = 0.02\ \Omega$.

TABLE 2. Comparison summary of the PLL-based (VCC) and PLL-less (VMDPC, LPV-PSC) grid-following inverters operating in different grid conditions.

Criteria	VCC			VMDPC			LPV-PSC		
Grid Type	Strong Grid	Weak Grid	Very Weak Grid	Strong Grid	Weak Grid	Very Weak Grid	Strong Grid	Weak Grid	Very Weak Grid
Full Control of Active Power	✓✓✓	✓	✗	✓✓	✓✓	✓	✓✓	✓✓	✓✓
Full Control of Reactive Power	✓✓✓	✓✓	✓	✓✓	✓	✓✓	✓✓✓	✓✓✓	✓✓✓
Stability	✓✓✓	✓	✗	✓✓✓	✓✓	✓	✓✓✓	✓✓✓	✓✓✓
Frequency Jump	✓✓✓	✓✓✓	✓✓	✓	✓	✓	✓	✓	✓
Phase Jump	✓✓✓	✓✓✓	✓✓	✓	✓	✓	✓✓	✓✓	✓✓
Grid Voltage Sag	✓✓	✓✓	✗	✓	✓	✓	✓✓✓	✓✓✓	✓✓✓
PCC Balanced Fault	✓✓	✓✓	✓✓	✓	✓	✓	✓✓✓	✓✓✓	✓✓✓

The performance of the controller is divided into four levels from superior to inferior: ✓✓✓ very well, ✓✓ good, ✓ marginally accepted, ✗ poor (or unstable)

the VMDPC is shown to have poor dynamic performance, as it takes quite a long time to reach the steady state after any change of the active/reactive power reference commands. It is worth mentioning that the VMDPC can be redesigned to provide a fast-tracking response by increasing the controller parameters. However, this solution will negatively impact the stability of the VMDPC in weak grid conditions, especially for high power applications where grid-connected inverters are as large as several MWs. Hence, such an inherent trade-off between the fast dynamic response in a strong grid and the stability in a weak grid limits the reliable operation of the VMDPC in different grid conditions.

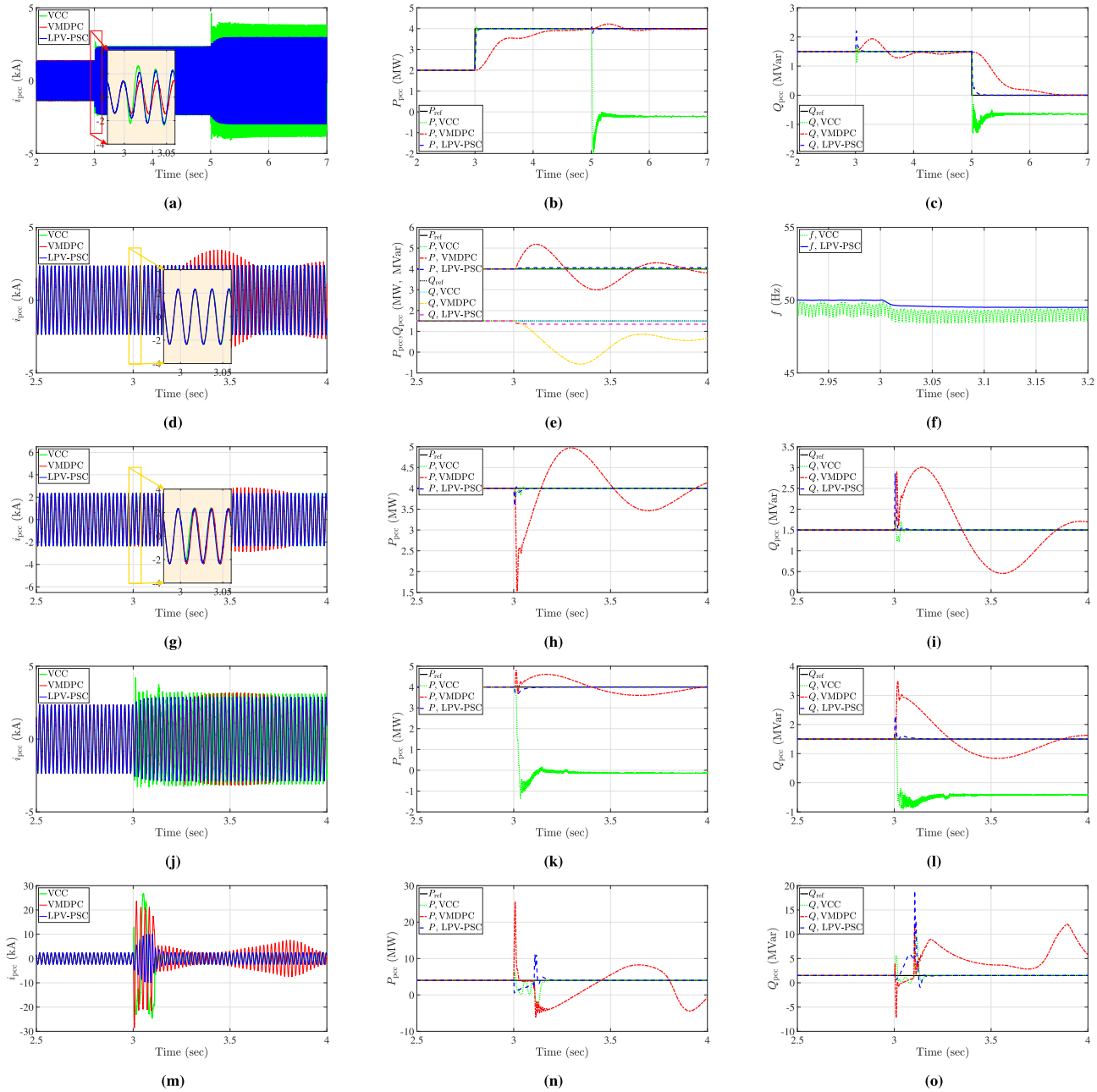

FIGURE 19. Response of the PLL-based (VCC) and PLL-less (VMDPC, LPV-PSC) grid-following inverters in very weak grid with SCR= 1.21 under: (a)-(c) step change in the active and reactive power references, (d)-(f) frequency jumps of the grid voltage source from 50 Hz to 49.5 Hz; (g)-(i) phase jumps in the grid voltage source equal to 15 degree; (j)-(l) permanent voltage sag in the grid voltage source equal to 20%V_g; (m)-(o) 3-ph fault to ground at the PCC for the a fault resistance equal to $R_f = 0.01\ \Omega$.

It is worth mentioning that there are certain limitations on controlling the active and reactive power via VMDPC and LPV-PSC strategies. On the one hand, the VMDPC approach needs the injection of a certain amount of reactive power in order to inject the rated active power in weak grid conditions. On the other hand, the LPV-PSC approach can be driven to instability when the inverter is expected to inject low amounts of active power. To overcome this limitation for the LPV-PSC, two possible solutions are suggested. The first solution is to inject a certain amount of reactive power when low real power is being injected. The second solution is to freeze the parameters of the power controller when the set-point of the active power is low. Hence, the stability of the LPV-PSC approach is ensured for low injections of low amounts of active without the need for reactive power support.

2) Control interaction stability: The three controllers, i.e., the VCC, VMDPC, and LPV-PSC, are stable in strong grid operation. It is worth mentioning that the stability

of the VCC mainly depends on the tuning of its SRF-PLL. In this study, the PLL was turned initially in strong grid conditions. Hence, it is unstable in very weak grid conditions, even though the controller was able to cope with weak grid operation due to the well-designed PLL.

3) Frequency jumps: The VCC outperforms the other two controllers. It is shown that a very robust operation against different frequency jumps in the grid voltage source. Although the LPV-PSC also shows good performance in such abnormal conditions, and it is able to track the grid frequency even faster than the VCC, the frequency jump results in a steady-state error in the injected active and reactive power by the VMDPC-based inverter, in which any drift in the grid frequency results in a slight steady-state increase and decrease in the output active and reactive power of the LPV-PSC, respectively. In contrast to VCC and LPV-PSC, the VMDPC is very sensitive to grid frequency deviations, where high overshoots in both the output active and reactive powers are generated in response to the frequency drifts, and it is found that the controller needs to move a long time that may exceed one second to recover to its operating status before the frequency disturbance.
4) Phase jumps: Both the VCC and LPV-PSC prove to be very robust to various phase jump values in the grid voltage source. The two controllers adapt to the phase changes very fast, where the effects of the phase jump are mitigated from the output current waveforms in less than one half fundamental cycle (<10) msec. However, the VMDPC is very sensitive to phase jumps in the grid voltage, where very high spikes in the output active and reactive powers are generated by the controller.
5) Grid voltage sags: It is found that the LPV-PSC outperforms the VCC and VMDPC. It produces the lowest transient current amplitude of the three control systems due to symmetrical voltage sags in the grid voltage source. Again, the VCC still performed better than the VMDPC for this abnormal controller.
6) PCC faults: During three-phase symmetrical faults at the PCC for different fault resistances, it is shown that the VMDPC fails to stay synchronized with the grid frequency during the transients and the time interval between the occurrence and clearance of a fault. On the other hand, VCC and LPV-PSC controllers are able to still synchronize with the grid frequency, and they maintain the amplitudes of the injected real and reactive power to the grid during the fault events much smaller than the injected powers by the VMDPC.

B. VCC, VMDPC, AND LPV-PSC IN (Very) WEAK GRID CONDITIONS

Overall, the LPV-PSC outperforms both the VCC and VMDPC controllers, as summarized below.

1) Control of active and reactive power: The LPV-PSC allows full control of the injected active and reactive power, independently, in both weak and very weak grid conditions. However, it is found that it is required to inject a certain amount of reactive power in order to support the active power control in weak grid operation. This phenomenon becomes more clear in very weak grid conditions in which the VCC fails completely to regulate its active power after reducing the reactive power injection to zero. For the VMDPC, setting the reactive power to zero affects directly the controller performance in the form of undamped oscillations in the inverter output active power.
2) Control interaction stability: Overall, the LPV-PSC is the most robust controller in both weak and very weak grid conditions, where the phase margin of the minor loop is always below the maximum limit of 180°. On the other hand, the VCC is unstable under a very weak grid. It is worth mentioning that the stability of both VCC and the VMDPC can be improved to cope even with a very weak grid operation if the controller parameters are redesigned to cope with such conditions. For example, the control parameters of the PI-controller of the SRF-PLL could be redesigned. Moreover, the power control parameters for the VMDPC power controller can be varied to cope with weak grid operations. However, there is always a trade-off between stability and good performance in both weak and strong grids.
3) Frequency and phase jumps: Similar to strong grid conditions, the VMDPC is the most sensitive controller to both the jumps in the frequency and phase of the grid voltage source. The VCC and LPV-PSC are very robust to these abnormal operations. Again, the LPV-PSC tracks the frequency variations faster than the VCC. However, these variations in the frequency produce steady-state errors in the output active and reactive power of the LPV-PSC.
4) Grid voltage sags and PCC faults: It is found that the LPV-PSC is the most stable controller under the permanent grid voltage sags and under the PCC faults. Compared to the three controllers, the VMDPC has the poorest dynamic performance under these abnormal fault conditions.

VI. CONCLUSION

This comparison study extensively assesses the performance of GFLIs equipped with three different control strategies, i.e., the conventional VCC, VMDPC, and LPV-PSC. The performance of the three controllers is tested and compared in strong and weak grid conditions under normal and severe operating conditions such as step change in power reference commands, frequency jump, phase jump, and sag in the PCC voltage. On the one hand, it is shown that the PLL-based VCC performs well in strong grid conditions. On the other hand, its performance deteriorates when connected to a weak grid

due to the instability issues posed by the PLL. This finding is also confirmed using impedance-based stability analysis in the dq reference frame based on the GNC. The two PLL-less controllers, i.e., the VMDPC and the LPV-PSC, remain stable in both strong and weak grid conditions. Nevertheless, the presented results prove the superiority of the LPV-PSC compared to the VMDPC. The frequency-domain analysis results confirm that the GFLIs equipped with LPV-PSC are more stable in the dq reference frame. Compared with the VCC and VMDPC, both the time-domain and frequency-domain results confirm the effectiveness of the recently proposed LPV-PSC scheme in terms of fast transient response, good tracking accuracy, and immunity to abnormal conditions, including frequency and SCR variations. Hence, it can be concluded that the LPV-PSC may be a promising control technique for GFLIs operating in both strong and weak grids.

REFERENCES

[1] E. Demirok, D. Sera, R. Teodorescu, P. Rodriguez, and U. Borup, "Clustered PV inverters in LV networks: An overview of impacts and comparison of voltage control strategies," in *Proc. IEEE Electr. Power Energy Conf. (EPEC)*, Oct. 2009, pp. 1–6.

[2] R. Teodorescu, F. Blaabjerg, M. Liserre, and P. C. Loh, "Proportional-resonant controllers and filters for grid-connected voltage-source converters," *IEE Proc.-Electr. Power Appl.*, vol. 153, no. 5, pp. 750–762, Sep. 2006.

[3] P. Piya, M. Ebrahimi, M. Karimi-Ghartemani, and S. A. Khajehoddin, "Fault ride-through capability of voltage-controlled inverters," *IEEE Trans. Ind. Electron.*, vol. 65, no. 10, pp. 7933–7943, Oct. 2018.

[4] P. Rodriguez, A. V. Timbus, R. Teodorescu, M. Liserre, and F. Blaabjerg, "Flexible active power control of distributed power generation systems during grid faults," *IEEE Trans. Ind. Electron.*, vol. 54, no. 5, pp. 2583–2592, Oct. 2007.

[5] M. Ciobotaru, V. G. Agelidis, R. Teodorescu, and F. Blaabjerg, "Accurate and less-disturbing active antiislanding method based on PLL for grid-connected converters," *IEEE Trans. Power Electron.*, vol. 25, no. 6, pp. 1576–1584, Jun. 2010.

[6] R. Teodorescu, M. Liserre, and P. Rodriguez, *Grid Converters for Photovoltaic and Wind Power Systems*, vol. 29. Hoboken, NJ, USA: Wiley, 2011.

[7] B. Bahrani, A. Karimi, B. Rey, and A. Rufer, "Decoupled dq-current control of grid-tied voltage source converters using nonparametric models," *IEEE Trans. Ind. Electron.*, vol. 60, no. 4, pp. 1356–1366, Apr. 2013.

[8] B. Bahrani, A. Rufer, S. Kenzelmann, and L. A. C. Lopes, "Vector control of single-phase voltage-source converters based on fictive-axis emulation," *IEEE Trans. Ind. Appl.*, vol. 47, no. 2, pp. 831–840, Mar. 2011.

[9] M. Reyes, P. Rodriguez, S. Vazquez, A. Luna, R. Teodorescu, and J. M. Carrasco, "Enhanced decoupled double synchronous reference frame current controller for unbalanced grid-voltage conditions," *IEEE Trans. Power Electron.*, vol. 27, no. 9, pp. 3934–3943, Sep. 2012.

[10] X. Wang, M. G. Taul, H. Wu, Y. Liao, F. Blaabjerg, and L. Harnefors, "Grid-synchronization stability of converter-based resources—An overview," *IEEE Open J. Ind. Appl.*, vol. 1, pp. 115–134, 2020.

[11] Y. Gui, X. Wang, H. Wu, and F. Blaabjerg, "Voltage-modulated direct power control for a weak grid-connected voltage source inverters," *IEEE Trans. Power Electron.*, vol. 34, no. 11, pp. 11383–11395, Nov. 2019.

[12] T. Noguchi, H. Tomiki, S. Kondo, and I. Takahashi, "Direct power control of PWM converter without power-source voltage sensors," *IEEE Trans. Ind. Appl.*, vol. 34, no. 3, pp. 473–479, May 1998.

[13] M. Zarif Mansour, M. H. Ravanji, A. Karimi, and B. Bahrani, "Linear parameter-varying control of a power-synchronized grid-following inverter," *IEEE J. Emerg. Sel. Topics Power Electron.*, vol. 10, no. 2, pp. 2547–2558, Apr. 2022.

[14] B. Bahrani, "Power-synchronized grid-following inverter without a phase-locked loop," *IEEE Access*, vol. 9, pp. 112163–112176, 2021.

[15] S. M. Hoseinizadeh, S. Ouni, H. Karimi, M. Karimi-Ghartemani, and K. L. Lian, "Comparison of PLL-based and PLL-less vector current controllers," *IEEE J. Emerg. Sel. Topics Power Electron.*, vol. 10, no. 1, pp. 436–445, Feb. 2022.

[16] J. Sun, "Impedance-based stability criterion for grid-connected inverters," *IEEE Trans. Power Electron.*, vol. 26, no. 11, pp. 3075–3078, Nov. 2011.

[17] T. Suntio, T. Messo, M. Berg, H. Alenius, T. Reinikka, R. Luhtala, and K. Zenger, "Impedance-based interactions in grid-tied three-phase inverters in renewable energy applications," *Energies*, vol. 12, no. 3, p. 464, Jan. 2019.

[18] R. Luhtala, T. Roinila, and T. Messo, "Implementation of real-time impedance-based stability assessment of grid-connected systems using MIMO-identification techniques," *IEEE Trans. Ind. Appl.*, vol. 54, no. 5, pp. 5054–5063, Sep./Oct. 2018.

[19] T. Roinila, T. Messo, and E. Santi, "MIMO-identification techniques for rapid impedance-based stability assessment of three-phase systems in DQ domain," *IEEE Trans. Power Electron.*, vol. 33, no. 5, pp. 4015–4022, May 2018.

[20] T. Suntio, T. Messo, and J. Puukko, *Power Electronic Converters: Dynamics and Control in Conventional and Renewable Energy Applications*. Hoboken, NJ, USA: Wiley, 2017.

[21] J. Mohammadpour and C. W. Scherer, *Control of Linear Parameter Varying Systems With Applications*. New York, NY, USA: Springer, 2012.

[22] R. D. Middlebrook, "Input filter considerations in design and application of switching regulators," in *Proc. IEEE Ind. Appl. Soc. Annu. Meeting*, Chicago, IL, USA, Oct. 1976, pp. 366–382.

[23] W. Zhou, R. E. Torres-Olguin, Y. Wang, and Z. Chen, "A gray-box hierarchical oscillatory instability source identification method of multiple-inverter-fed power systems," *IEEE J. Emerg. Sel. Topics Power Electron.*, vol. 9, no. 3, pp. 3095–3113, Jun. 2021.

[24] W. Cao, Y. Ma, L. Yang, F. Wang, and L. M. Tolbert, "D–Q impedance based stability analysis and parameter design of three-phase inverter-based AC power systems," *IEEE Trans. Ind. Electron.*, vol. 64, no. 7, pp. 6017–6028, Jul. 2017.

[25] W. Zhou, R. E. Torres-Olguin, M. K. Zadeh, B. Bahrani, Y. Wang, and Z. Chen, "Electromagnetic oscillation origin location in multiple-inverter-based power systems using components impedance frequency responses," *IEEE Open J. Ind. Electron. Soc.*, vol. 2, pp. 1–20, 2021.

[26] B. Wen, R. Burgos, D. Boroyevich, P. Mattavelli, and Z. Shen, "AC stability analysis and dq frame impedance specifications in power-electronics-based distributed power systems," *IEEE J. Emerg. Sel. Topics Power Electron.*, vol. 5, no. 4, pp. 1455–1465, Dec. 2017.

[27] N. Mohammed, M. Ciobotaru, and G. Town, "Fundamental grid impedance estimation using grid-connected inverters: A comparison of two frequency-based estimation techniques," *IET Power Electron.*, vol. 13, no. 13, pp. 2730–2741, 2020.

[28] N. Mohammed and M. Ciobotaru, "Fast and accurate grid impedance estimation approach for stability analysis of grid-connected inverters," *Electr. Power Syst. Res.*, vol. 207, Jun. 2022, Art. no. 107831.

[29] N. Mohammed, M. Ciobotaru, and G. Town, "Online parametric estimation of grid impedance under unbalanced grid conditions," *Energies*, vol. 12, no. 24, p. 4752, Dec. 2019.

[30] Q. Qian, S. Xie, L. Huang, J. Xu, Z. Zhang, and B. Zhang, "Harmonic suppression and stability enhancement for parallel multiple grid-connected inverters based on passive inverter output impedance," *IEEE Trans. Ind. Electron.*, vol. 64, no. 9, pp. 7587–7598, Sep. 2017.

[31] W. Zhou, Y. Wang, R. E. Torres-Olguin, and Z. Chen, "Effect of reactive power characteristic of offshore wind power plant on low-frequency stability," *IEEE Trans. Energy Convers.*, vol. 35, no. 2, pp. 837–853, Jun. 2020.

NABIL MOHAMMED (Member, IEEE) received the bachelor's degree (Hons.) in electrical power engineering from Tishreen University, in 2013, the M.Eng. degree in electrical engineering from Universiti Teknologi Malaysia (UTM), in 2017, and the Ph.D. degree in power electronics from Macquarie University, Australia, in 2022. During the Summer of 2019, he was a Visiting Researcher at the Department of Energy Technology, Aalborg University, Denmark. He is currently a Postdoctoral Research Fellow with Monash University, Australia. His research interests include power electronic converters, renewable energy generation and integration in power systems, microgrids, energy storage and management systems, and modeling and control of electric systems.

WEIHUA ZHOU (Member, IEEE) was born in Anhui, China, in 1993. He received the B.Eng. degree in electrical engineering from the Honors College, Northwestern Polytechnical University, Xi'an, China, in 2014, the M.Sc. degree in electrical engineering from the School of Automation, Northwestern Polytechnical University, in 2017, and the Ph.D. degree in power electronics from the Department of Energy Technology, Aalborg University, Aalborg, Denmark, in 2020.

From November 2015 to May 2016, he was a Junior Research Assistant at the Department of Mechanical and Automation Engineering, The Chinese University of Hong Kong, Hong Kong. From August 2020 to November 2020, he was a Visiting Scholar at the Department of Marine Technology, Norwegian University of Science and Technology, Trondheim, Norway. In 2021, he was a Postdoctoral Fellow at the Department of Electrical Engineering, KU Leuven, Leuven, Belgium. He is currently a Postdoctoral Research Fellow with the Department of Electrical and Computer Systems Engineering, Monash University, Melbourne, Australia. His research interests include modeling and control of power electronic converters, energy storage systems, and stability analysis and enhancement of power electronic- and underground cable-based modern power systems.

BEHROOZ BAHRANI (Senior Member, IEEE) received the B.Sc. degree from the Sharif University of Technology, Tehran, Iran, in 2006, the M.Sc. degree from the University of Toronto, Toronto, ON, Canada, in 2008, and the Ph.D. degree from the École Polytechnique Fédérale de Lausanne (EPFL), Lausanne, Switzerland, in 2012, all in electrical engineering. From September 2012 to September 2015, he was a Postdoctoral Fellow at EPFL; Purdue University, West Lafayette, IN, USA; the Georgia Institute of Technology, Atlanta, GA, USA; and the Technical University of Munich, Munich, Germany. Since 2015, he has been with Monash University, Melbourne, Australia, where he is currently a Senior Lecturer and the Director of the Grid Innovation Hub. His research interests include control of power electronic converters, their applications in power systems, and grid integration of renewable energy resources.